Progress in Oceanography
February 2024, Volume 221, Pages 103191 (15p.)
https://doi.org/10.1016/j.pocean.2023.103191 https://archimer.ifremer.fr/doc/00868/98037/

Investigation of hydrothermal activity in the South West Indian Ridge region using Ra isotopes and ^{227}Ac as tracers

Léon Morgane [1, *], Van Beek Pieter [1, *], Sanial Virginie [2, *], Baudet Corentin [3], Charette Matthew A. [4], Souhaut Marc [1], Vivier Frédéric [5], Kestenare Elodie [1], Jeandel Catherine [1], Planquette Helene [3]

[1] Laboratoire d'Etudes en Géophysique et Océanographie Spatiales (LEGOS), Université de Toulouse, CNES/CNRS/IRD/Université Toulouse III Paul Sabatier (UT3), Toulouse, France
[2] Université de Toulon, Aix Marseille Univ., CNRS, IRD, MIO, Toulon, France
[3] CNRS, Univ Brest, IRD, Ifremer, LEMAR, F-29280, Plouzané, France
[4] Department of Marine Chemistry and Geochemistry, Woods Hole Oceanographic Institution, Woods Hole, MA 02543, USA
[5] LOCEAN-IPSL, CNRS, Sorbonne Université, Paris, France

* Corresponding authors : email addresses : morgane.leon@univ-tlse3.fr ; pieter.van-beek@univ-tlse3.fr ; virginie.sanial@univ-tln.fr

Abstract :

Hydrothermal vents have been shown to be important vectors for various chemical elements into the ocean. However, both the intensity of the chemical fluxes associated with these systems and the fate of the chemical elements along the plume are still largely overlooked. At two stations located above the South West Indian Ridge (SWIR), we investigate the distributions of the Ra quartet (223Ra, 224Ra, 226Ra and 228Ra) and 227Ac that have been used as tracers of hydrothermal activity. While the vertical distributions of 226Ra, 228Ra and 227Ac do not show a clear enrichment at depth, unusual signatures of excess 223Ra and 224Ra near the seafloor are attributed to the presence of a hydrothermal activity. The discrepancy observed between the different isotopes is attributed to different chemical reactivity when seawater circulates within the crust and/or to different regeneration rates within the fluid. A 1D diffusion model applied to the vertical profiles of short-lived Ra isotopes provided an estimation of the vertical eddy diffusivity coefficients (KZ) between 38 cm2 s-1 and 149 cm2 s-1. These high values suggest strong mixing likely favored by the complex bathymetry in the region. By combining these KZ with the vertical gradient of dissolved Fe (dFe), we estimate a vertical flux of dFe that ranges from 139 to 1173 nmol m-2 d-1. These results confirm that low-expansion-rate ridges could be significant sources of dFe to the deep ocean.

Highlights

► Short-lived Ra isotopes highlight the presence of a hydrothermal activity on the SWIR. ► The hydrothermal system is located at a distance < 30km of the investigated stations. ► A strong vertical mixing is observed (Kz from 38 up to 149 cm^2 s^{-1}) ► A large dFe vertical flux from 552 up to1173 nmol m^{-2} d^{-1} are estimated.

Keywords : Radium isotopes, 227Ac, SWIR, Hydrothermalism, Vertical eddy diffusivity coefficient, Chemical fluxes

1 Introduction

Since their discovery in the late 1970s (Corliss et al., 1979), hydrothermal vents have been studied worldwide from biological, chemical and geological perspectives (Wolery and Sleep, 1976; Humphris et al., 1995; German and Von Damm, 2003; Baker et al., 2013). We distinguish two main types of hydrothermal systems. At spreading ridges, magma chambers that contain molten rock (basaltic and/or gabbroic) discharge lavas onto the ocean floor during volcanic eruption events, producing black smokers and associated diffuse flows systems. Other hydrothermal vents, known as mafic or ultramafic systems, are supplied by fault activities and observed tens of kilometers off-axis (Martin et al. 2008).

When seawater percolates through the fractured oceanic crust, it interacts with the surrounding rocks, which modifies significantly the seawater chemical composition (Krishnaswami et al., 1982). For example, temperature, salinity, pH as well as the composition of the solid phase control the partitioning of radionuclides from the U-Th series between the aqueous and solid phases. While in marine systems radium (Ra) is easily released from surfaces or particles due to the high ionic strength and is then found mostly in the dissolved phase, thorium (Th) and protactinium (Pa) are strongly reactive to particles and preferentially adsorb onto mineral surfaces (Cochran, 1982). ^{227}Ac is also believed to have a significant affinity for particles and may be partially adsorbed onto mineral surfaces (Moore et al., 2008; Kipp et al., 2015), but due to its higher solubility relative to Th and Pa, ^{227}Ac is partially released into the dissolved phase once it is produced by the radioactive decay of ^{231}Pa (Anderson et al., 1983; Nozaki, 1984, 1993). Near mid ocean ridges, radium activities increase in the dissolved phase in relationship with temperature and the acidic nature of seawater (Edmond et al., 1979, 1982; Campbell et al., 1988; Kadko and Moore, 1988; Kipp et al., 2015). Radium isotopes that display different half-lives (^{224}Ra, 3.66 days; ^{223}Ra, 11. 4 days; ^{228}Ra, 5.75 years; ^{226}Ra, 1600 years) have thus been widely used to trace

hydrothermal plumes (Kadko and Moore, 1988; Kadko, 1996; Kadko and Butterfield, 1998; Kadko et al., 2007; Moore et al., 2008; Kipp et al., 2018; Neuholz et al., 2020a; Moore et al., 2021). ^{228}Ra, produced by the radioactive decay of ^{232}Th ($t_{1/2}$ = 1.405 x 10^{10} years) is a preferred tracer to study the crustal residence time of fluids (Kadko and Moore, 1988; Kadko, 1996; Kadko and Butterfield, 1998; Kadko et al., 2007). More recent studies used the short-lived isotopes, ^{223}Ra and ^{224}Ra - produced by radioactive decay of ^{227}Ac ($t_{1/2}$ = 21.8 years) and ^{228}Th ($t_{1/2}$ = 1.9 years), respectively - in order to constrain seawater residence time and trace element fluxes around hydrothermal vents at shorter time scales (Kadko et al., 2007; Moore et al., 2008; Kipp et al., 2018; Neuholz et al., 2020a; Moore et al., 2021). More specifically, Moore et al. (2008) were the first to observe high activities of ^{223}Ra in excess of its parent ^{227}Ac in the low temperature hydrothermal vent system of Puna Ridge (Hawaii, USA), thus demonstrating that ^{223}Ra was a powerful tracer of low-temperature vents. Because of the particle affinity of ^{231}Pa and to a lesser extent of ^{227}Ac, the ^{227}Ac activities observed in the vicinity of low temperature ridges are expected to be similar or even lower than those in the ambient waters (Moore et al., 2008; Geibert et al., 2008). However, Kipp et al. (2015) have shown that hydrothermal vents could be a source of this element to the deep ocean and thus suggested that ^{227}Ac could be used as a tracer of these systems.

It is now well established that hydrothermal vents constitute significant vectors for various gases and trace elements into the sea (Von Damm, 1990; Elderfield and Schultz, 1996; German and Seyfried, 2014). In the vicinity of these systems, waters may be enriched in various chemical elements and unique ecosystems develop (Ramirez-Llodra et al., 2010; Lemaitre et al., 2020). Fast spreading ridges are thought to be important contributors to the oceanic iron inventory (e.g., Tagliabue et al., 2010) while slow spreading ridges have long been considered as less significant and thus have been less explored, although they represent about half of the global mid ocean ridge axis (Tagliabue et al., 2010). Interestingly, Saito et al. (2013) reported an upward revision of estimated vent contribution of dissolved Fe (dFe) in the slow spreading rate Mid-Atlantic Ridge and suggest that the ridge spreading rate is not the first order control of Fe flux from hydrothermal vents. The impact of hydrothermal systems on the oceanic biogeochemical cycles depends not only on the magnitude of the system, but also on the processes that control the persistence and the transport of the chemical elements, which can extend thousands of km from the source, as was shown for Fe (Resing et al., 2015; Tagliabue et al., 2022, Neuholz et al., 2020a,b). In the Southern Ocean, inputs from the various hydrothermal vents to the surface may be favored by topography upwelling features (Walter et al., 2010). However, the remoteness and extreme conditions of this region complicate the investigation of hydrothermal vent localization and the fate of their plumes (Ardyna et al., 2019). Because the Southern Ocean is the largest iron-limited region of the global ocean, making phytoplankton highly sensitive to Fe inputs (Boyd and Ellwood, 2010), it was proposed that upwelled hydrothermally influenced deep waters could promote phytoplankton blooms in this region (Tagliabue et al., 2010; Ardyna et al., 2019; Schine et al., 2021). However, Lough et al. (2023) highlight the complexity of tracing hydrothermal Fe supply due to uncertainties associated with the at-sea sampling strategy and the temporal nature of plume dynamics. Hence it is important to constrain the localization, the transport rate, as well as the fluxes of trace elements and isotopes emanating from slow spreading ridge, especially in this region of the world's ocean.

The South West Indian Ridge (SWIR) is among the world's slowest spreading ridges with a full spreading rate of ~14-16 mm y^{-1} (Patriat et al., 1997). To the present day, tens of active hydrothermal vents have been identified along the SWIR, from the Westernmost part, off the coast of South Africa (Baker et al., 2004), to the Easternmost part, off the coast of Madagascar (German

et al., 1998; Tao et al. 2009, 2014; Han et al. 2010; Liao et al., 2018). The presence of a hydrothermal activity was suspected from a previous cruise conducted in the region between Prince Edward (35°E) and Eric Simpson (40°E) fracture zones (SWIFT cruise, Jan-March 2001; Humler et al., 2001). During this latter cruise, various geophysical data (bathymetry, magnetism and gravity) were acquired along the ridge (Humler, 2001). Further, Sato et al. (2013) highlighted magmatic activity in this region by conducting a geophysical survey between the Prince Edward and Eric Simpson fracture zones (latitude 35 – 40° E). Following these previous studies, a detailed bathymetric survey was conducted in this region of the SWIR during the SWINGS cruise and two stations where hydrothermal activity was suspected were studied. In the present study, we investigated the distribution of the four radium isotopes and ^{227}Ac at these two stations. Ra isotopes and ^{227}Ac were used as tracers i) to investigate on the presence of a hydrothermal activity, ii) to quantify the vertical eddy diffusivity coefficient K_Z and iii) to estimate the vertical flux of dFe associated with these systems.

2 Materials and Methods

2.1 Study area and geological settings

The SWINGS cruise took place on the R/V *Marion Dufresne* from January to March 2021 (http://dx.doi.org/10.17600/18001925) as part of the GEOTRACES program (GA01section). This cruise was designed to study the distribution of trace elements and isotopes in the Indian sector of the Southern Ocean along a section between South Africa and Heard Island. Part of the investigated transect was explored for bathymetry (see section 2.2.) and two stations (Station 14, 1388 m, 44°51.690 S, 36°10.460 E; Station 15, 1770 m, 44°51.178 S, 36°13.841 E) were studied over the SWIR to investigate the presence of hydrothermal activity, following a previous cruise that was conducted in this specific region (Humler, 2001).

The SWIR is a major plate boundary separating Africa and Antarctica for more than 100 Ma. The ridge extends 7700 km from the Bouvet triple junction at 55º S, 1º W to the Rodrigues triple junction at 26º S, 70º E and due to its ultra-slow spreading rate, the SWIR is one of the most rugged topographies of all the world's ridges (DeMets et al., 1990). Based on magma supply, the SWIR can be divided into three sections were several hydrothermal fields have already been discovered: (i) the western region, located west of the Andrew Bain transform fault, which has a moderate averaged magma supply, (ii) the middle region, located between Andrew Bain (~ 31°E) and Gallieni (~52°E) transform fault, which has a strong averaged magma supply and (iii) the eastern region, located east of the Gallieni transform fault, which has a weak averaged magma supply (Sauter and Cannat, 2010; Tao et al., 2023). The middle region is overall hotter, has a thicker oceanic crust and displays locally strong magma supply areas, discretely distributed along the section (Tao et al., 2023). It has been shown that local enhanced magmatism promotes hydrothermal circulation (Tao et al., 2013; Chen et al., 2018). The Dunquiao hydrothermal field located in the middle region - where stations 14 and 15 were investigated - is described as a typical local strong magma supply hydrothermal field with intense magmatic activity (Tao et al. 2012).

A first cruise (SWIFT project, for South West Indian French Transect), initiated research in 2001 in the shallowest part of the SWIR between the Andrew Bain fracture zone and the Gallieni fracture zone (middle section), using a multibeam sonar bathymetry gridded at 100 m (Humler, 2001; https://doi.org/10.17882/59494). Through dredging of the seafloor - in the same area as station 14

investigated during the SWINGS project - pillow basalts, few pieces of ropey lava flows and traces of biological activity were observed (e.g. at the SWIFT station DR05 located 44°51 S, 36°10 E, 1320 m). The section investigated here during the SWINGS project for bathymetry (see section 2.2) is part of a larger segment (PE-1) studied by Sato et al. (2013) who conducted geophysical surveys including bathymetry, gravity and magnetism on the SWIR in the vicinity of the Marion hotspot along several segments between Prince Edward and Eric Simpson fracture zones. Segment PE-1 was shown to be dominated by local magma supply, similarly to the Dunquiao hydrothermal field (50.5°E; Tao et al., 2012). Note that in the eastern part of the SWIR, other hydrothermal fields such as Tiancheng (active, low temperature hydrothermal field) and Tianzuo (inactive hydrothermal field) were also observed in magmatic zones (Chen et al., 2018; Tao et al. 2023). In the PE-1 segment, the crust was estimated to be 7–8 km thick in the region investigated here (that is, around the center of segment PE-1), the area of thick crust generally overlapping the area of shallow topography. Sato et al. (2013) reported a mean spreading rate of segment PE-1 of 16.5 mm a^{-1}, which allows to classify the investigated region as an ultra-slow spreading ridge. Sato et al. (2013) concluded that it may not be excluded that the magmatic activity of segments PE could be influenced by the Marion hotspot. No specific geological observations were conducted during the SWINGS cruise.

2.2 Bathymetric exploration

During the SWINGS cruise, a high-resolution (15 m) multibeam sonar bathymetric exploration was performed during 25 hours above the SWIR on an area of approximately 200 km² (Fig. 1; https://doi.org/10.17882/89462) between the prince Edward fracture zone and the Eric Simpson fracture zone (36°05E to 36°21E). Data were acquired with a hull-mounted multibeam echosounder Kongsberg EM122 12 kHz using an optimized configuration for bathymetry data collection. Acoustic data were processed with the GLOBE software (https://doi.org/10.17882/70460) to provide a 15 m resolution bathymetry map. The presence of a consistent geomorphological feature (volcano shape) detected by the sonar survey has led to further investigate both stations 14 and 15. The location of the two stations is reported on the high-resolution bathymetric map (Fig. 1). The two stations are located on the flank of the ridge, about 5 km away from each other.

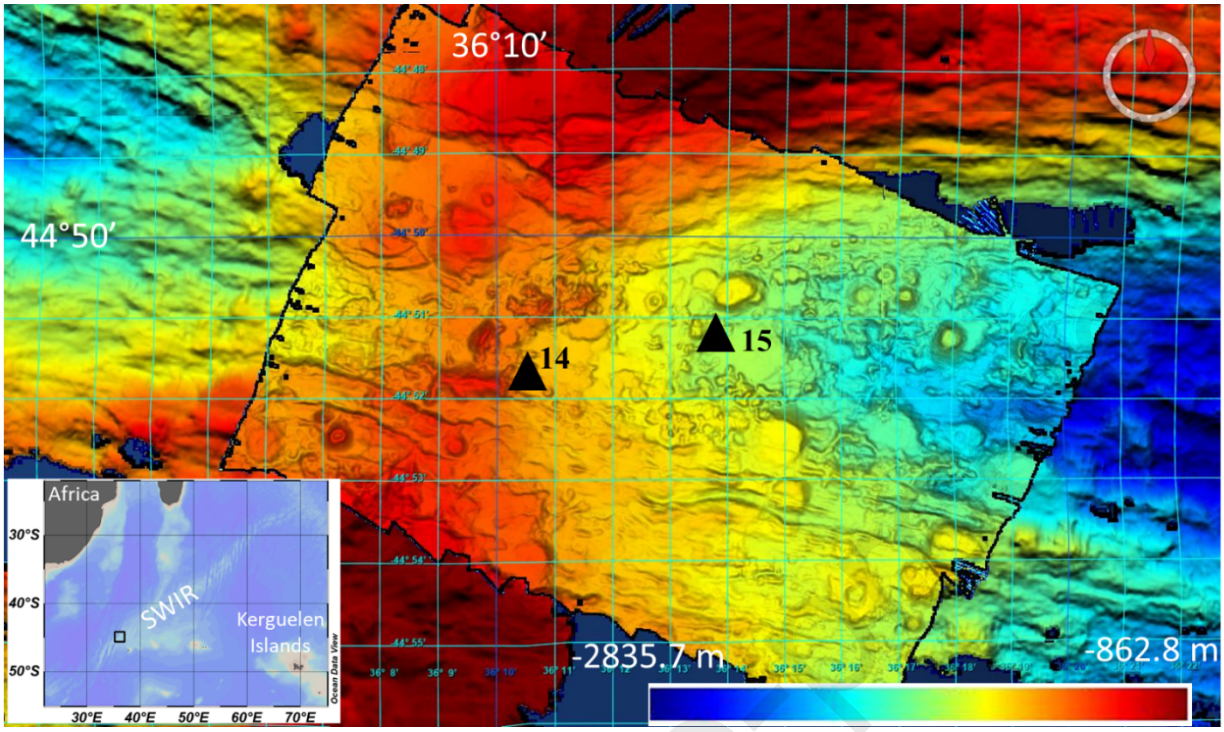

Figure 1. High resolution (15 m) bathymetry map of the SWIR segment investigated during SWINGS cruise. The locations of stations 14 and 15 are shown as black triangles on the map. The location of the segment is shown on the bottom left panel (black square). The color bar shows the bathymetry that ranges from 862.8 to 2835.7 m.

2.3 Sampling method

Acrylic cartridges impregnated with MnO_2 (so called, Mn-cartridges) were prepared according to the protocol established by Henderson et al. (2013). These Mn-cartridges were mounted on McLane in-situ pumps (ISP) to preconcentrate dissolved Ra isotopes and ^{227}Ac from large volumes of seawater at various depths in the water column. Seawater first passed through Supor (0.8 µm pore size) or QMA (Whatman© 1 µm pore size) filters before passing through the Mn-cartridges. Eight ISP were deployed at station 14 and six ISP were deployed at station 15 for 3 hours of pumping, thus filtrating through the Mn-cartridges between 427 and 677 L of seawater. Note that the sampling resolution was increased near the seafloor due to the expected presence of a hydrothermal activity. Except for the three shallowest pumps at station 14 (50 m, 200 m, 900 m), two Mn-cartridges were mounted in series in order to provide information on the yield of ^{227}Ac fixation, following Henderson et al. (2013) and Le Roy et al. (2019).

Water samples were also collected from Niskin bottles (ca. 12 L) mounted on a rosette and deployed at the same depths as the ISPs. These samples were designed to collect dissolved ^{226}Ra. Because ^{226}Ra displays higher activities in seawater than ^{223}Ra, ^{224}Ra and ^{228}Ra, the analysis of ^{226}Ra can be conducted in relatively small volumes (~10-12 L). These samples were then passed by gravity through 10 g of acrylic fibers impregnated with MnO_2 (so called, Mn-fibers) at a flow rate < 0.5 L.min^{-1} to quantitatively adsorb ^{226}Ra isotopes. By doing so, we assume that the Mn-fibers scavenge 100% of Ra (Moore and Reid, 1973).

To sample dissolved iron (dFe), GO-FLO bottles were mounted on a trace metal clean rosette. All manipulations of the GO-FLO bottles occurred into a clean container dedicated for sampling trace elements. Seawater was filtered on-line through a 0.45 µm polyethersulfone filter (Supor) and collected in acid-cleaned 60 mL LDPE bottles. The samples were then acidified within 24h after collection with HCl (ultrapure grade, Merck, final pH 1.8) (Baudet et al., submitted).

2.4 Analytical method

Both Mn-cartridges and Mn-fibers were analyzed using four Radium Delayed Coincidence Counter (RaDeCC) systems (Moore, 2008). All samples were analyzed for 6 to 24 hours by flushing the RaDeCC system every 3 hours during 5 to 10 minutes with air, before reintroducing helium into the system. Because of their short half-life, ^{224}Ra and ^{223}Ra were measured on board, within a few hours of sample collection. This first measurement provides the total ^{224}Ra ($^{224}Ra_{tot}$) and ^{223}Ra ($^{223}Ra_{tot}$) activities. A second measurement was conducted 21 days after sampling, to quantify the ^{224}Ra supported by ^{228}Th in the samples. These supported activities were then subtracted from the $^{224}Ra_{tot}$ activities to determine excess ^{224}Ra (denoted $^{224}Ra_{ex}$). A third counting was performed about 90 days after sample collection to quantify the ^{223}Ra supported by ^{227}Ac. In the same way, these supported activities were then subtracted from the $^{223}Ra_{tot}$ activities to determine excess ^{223}Ra (denoted $^{223}Ra_{ex}$). In the following, the activities reported for short-lived Ra isotopes are thus $^{223}Ra_{ex}$ and $^{224}Ra_{ex}$. Error propagation calculations followed Garcia-Solsona et al. (2008). RaDeCCs were calibrated with Mn-cartridges and Mn-fibers impregnated with ^{232}Th standards. The detection efficiencies of the RaDeCCs for ^{223}Ra and ^{227}Ac were determined following Moore and Cai, (2013). In order to quantify ^{227}Ac, between 3 and 5 analyses were performed for each sample using RaDeCC and the ^{227}Ac activities reported here correspond to the mean of these different analyses (Léon et al., in prep.). The yield of ^{227}Ac fixation onto the Mn-cartridges was determined from the two Mn-cartridges placed in series, as was done in the past for various radionuclides (Mann and Casso, 1984; Livingston and Cochran, 1987; Baskaran et al., 1993; van der Loeff and Moore, 1999; Le Roy et al., 2019). Errors reported for the ^{227}Ac activities correspond to the standard deviation of the mean (1SD).

The analyses of the ^{226}Ra activities on Mn-fibers were performed using a ^{222}Rn extraction line (daughter of ^{226}Ra, half-life: 3.8 days) followed by alpha scintillation counting system. Briefly, the Mn-fibers are first placed in PVC cartridges (Peterson et al., 2009) and then flushed with helium for five minutes at a flow rate of 250 min L^{-1}. These cartridges are then sealed and held about one week (minimum of 5 days) before being analyzed to await radioactive regrowth of ^{222}Rn. The ^{222}Rn is then flushed out of the cartridge and cryo-trapped in a copper tube cooled with liquid nitrogen. After about 15 minutes of ^{222}Rn accumulation in the copper tube, the copper tube was heated and the ^{222}Rn was guided by helium into a Lucas cell, an airtight chamber covered with silver activated zinc sulfide on its inner walls which emit a photon when struck by an alpha particle (Key et al., 1979; Lucas, 1979; Peterson et al., 2009). The analysis of these cells takes place 3h after sealing in order to reach the secular equilibrium of the ^{222}Rn daughters. Cells are counted for several hours (from 3 to 6 hours) in a Rn counting system (model AC/DC-DRC-MK 10-2). Uncertainties reported for ^{226}Ra include counting statistics and uncertainty on the detection efficiencies (1SD).

The analyses of the ^{226}Ra activities on Mn-cartridges were performed using a large, low background, high efficiency, well-type germanium gamma spectrometer (SAGe-Well, MIRION-

CANBERRA) placed underground at the LAFARA laboratory in the French Pyrénées. The volume of the germanium crystal is 450 cm^3 and the diameter of the well is 32 mm. The facility is located under 85 m of rock that protect the detectors from cosmic radiations, thus providing a very low background (van Beek et al., 2013). Prior to analysis, Mn-fibers were pressed into plastic tubes while Mn-cartridges were ashed (to reduce the volume) before being placed in the tubes. The tubes were then sealed to prevent any loss of ^{222}Rn from the samples and were analyzed 3 weeks after the sample preparation to make sure that radioactive equilibrium is reached between ^{226}Ra, ^{222}Rn and the following daughters. ^{226}Ra activities were determined using the ^{214}Pb (295 keV and 352 keV) and ^{214}Bi (609 keV) peaks after 5 days of counting. We used the APEX software (MIRION-CANBERRA) to quantify these activities. Uncertainties reported for ^{226}Ra include counting statistics and uncertainty on the detection efficiencies (1SD).

Here, we report $^{223}Ra_{ex}/^{226}Ra$, $^{224}Ra_{ex}/^{226}Ra$, $^{228}Ra/^{226}Ra$ and $^{224}Ra_{ex}/^{228}Ra$ ratios determined in Mn-cartridges (Table 1). By combining these ratios with the ^{226}Ra activities determined using Mn-fibers (that quantitatively remove Ra from seawater), we could determine $^{223}Ra_{ex}$, $^{224}Ra_{ex}$ and ^{228}Ra activities in the water columns at stations 14 and 15. The vertical profiles of ^{227}Ac activities were built by analyzing ^{227}Ac in Mn-cartridges placed in series, following the protocol described in Le Roy et al. (2019).

In order to analyze the total dFe concentrations, samples were stored at room temperature and measured at LEMAR in Brest, 12 months after sampling. dFe concentrations were analyzed using a preconcentration system seaFAST-picoTM coupled to a high-resolution magnetic sector field inductively-coupled plasma mass spectrometer (SF-ICP-MS, Element XR – Pôle Spectrométrie Océan, Brest) following Tonnard et al., (2020). An air blank (no sample uptaken but with contribution of all reagents) of 0.14 ± 0.05 nmol L^{-1} was used. The vertical profiles of dFe can be found in Baudet et al. (submitted).

2.5 Ancillary data

Hydrographic profiles were collected with a Seabird SBE911plus conductivity-temperature-depth (CTD) probe with an accuracy of ±0.001° C for temperature and ±0.003 mS/cm for conductivity. Dissolved oxygen concentration was measured with a Seabird SBE43 sensor attached to the rosette. Oxygen data were further calibrated with ex-situ titrations (Winkler method) from water samples taken at stations regularly spaced during the cruise. Beam transmittance was measured with a WET Labs C-Star transmissometer. Velocity profiles were collected at each station from a pair of lowered-acoustic Doppler current profilers (LADCP) mounted on the rosette, composed of an up-looking and a down-looking Workhorse Sentinel ADCP from Teledyne RD Instruments operating at 300 kHz and 150 kHz, respectively. LADCP data were processed based on the velocity inversion method (Visbeck,2002) using the IFM-GEOMAR/LDEO software (Visbeck and Krahmann, version 11.0). Other ancillary data include daily altimeter satellite gridded sea-surface height and derived surface geostrophic currents at 0.25° spatial resolution from the Copernicus Marine Environment Monitoring Service (CMEMS), and daily horizontal current fields at 46 vertical levels from the state of the art GLORYS12 global eddy-resolving ocean and sea ice reanalysis at 1/12° horizontal resolution implemented in the framework of the CMEMS (Lellouche et al 2021). GLORYS12 assimilates a variety of observations including satellite sea level anomaly, surface temperature and sea ice concentration, as well as available hydrographic in situ data. Barotropic tidal currents were estimated separately with the Tide Model Driver (TMD v2.5) package developed by Earth and Space Research, using

the TPXO9v5 global tide model with 14 harmonic constituents, assimilating satellite altimeter data (Egbert and Erofeeva, 2002).

3 Results

3.1. Hydrography and circulation above the SWIR

The vertical profiles of temperature, salinity, beam transmission and oxygen are reported in Fig 2. For both stations, the temperature decreased rapidly over the first 200 meters and then more slowly from about 5°C to 2-3°C near the bottom. Salinity increases almost constantly with depth, with notably a high increase from around 300 m. Beam transmission, which can reflect the presence of particulate matter, increases away from the surface and then stabilizes at a value close to 85.5% along the vertical profiles. The O_2 concentration remains almost stable from the surface to 200 m (~270 $\mu m.kg^{-1}$), then decreases regularly up to 1000 m where it reaches approximately 170 $\mu m.kg^{-1}$ near the bottom. Except for a slight increase (0.02) of salinity at station 14 in 70 m thick bottom boundary layer, no clear pattern was observed in salinity, temperature, O_2 or beam transmission that could indicate the presence of a hydrothermal activity at these two stations (Fig. 2). Temperature and salinity observed here suggest a surface mixed layer of about 100 m at Station 14 and about 70 m at station 15. The different water masses encountered were identified. The Antarctic Intermediate Water (AAIW), characterized by temperature between 0 and 5°C and salinity about 33.5 - 34.5, was found down to 800 m. The Circumpolar Deep Water (CDW), with a neutral density larger than 27.5 kg m^{-3}, lies just below the AAIW layer and can be decomposed into (i) Upper Circumpolar Deep Water (UCDW) and (ii) Lower Circumpolar Deep Water (LCDW), which was found at depths greater than 1350 m (station 15). The stations were too

shallow to observe Antarctic Bottom Water (AABW), usually present below 3000 m (Park and Gamberoni, 1997).

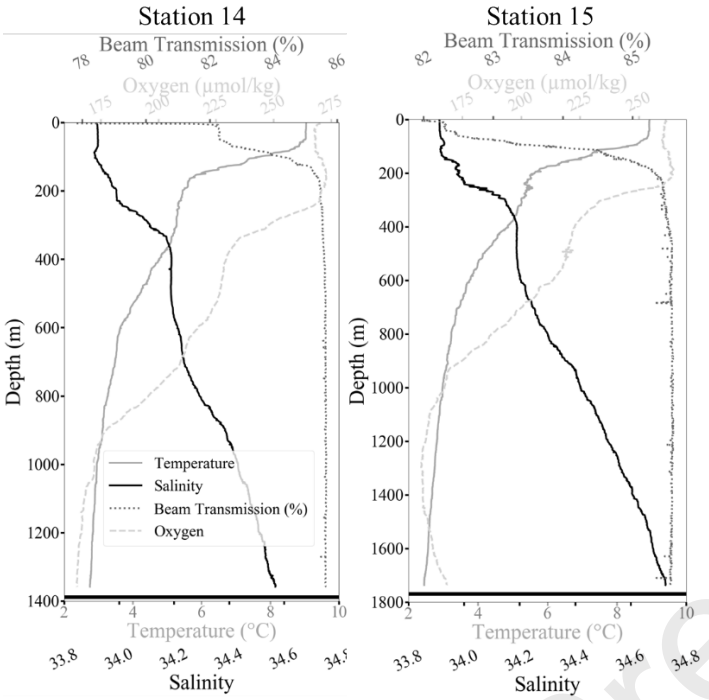

Figure 2: Temperature (grey full line), salinity (black full line), beam transmission (black dotted line) and oxygen (grey dashed line) profiles at stations 14 (left panel) and 15 (right panel). The horizontal black lines represent the bottom depth for each station.

The concurrent surface geostrophic velocity field derived from satellite altimetry averaged between 25 and 29 January (Fig. 3a) indicates that the study area was away from the fronts and deep-reaching jets associated with the Antarctic Circumpolar Current: stations 14 and 15 were located at the center of a weak anticyclonic circulation pattern straddling the ridge, a location associated with a low velocity (< 5 cm s^{-1}). The horizontal velocity field at successive depths is provided by the GLORYS12 reanalysis (Fig. 3b-d). The latter was assessed by comparing the velocity field at 190 m depth, i.e., below the Ekman layer, with the surface geostrophic velocity field from altimetry, demonstrating a reasonable agreement in the region of interest with, however, a slight westward shift of the anticyclonic circulation pattern mentioned above (Fig. 3b). Below

1000 m depth, horizontal currents at stations 14 and 15 are smaller than at the near surface, but remain consistently northeastwards (Fig. 3c-d).

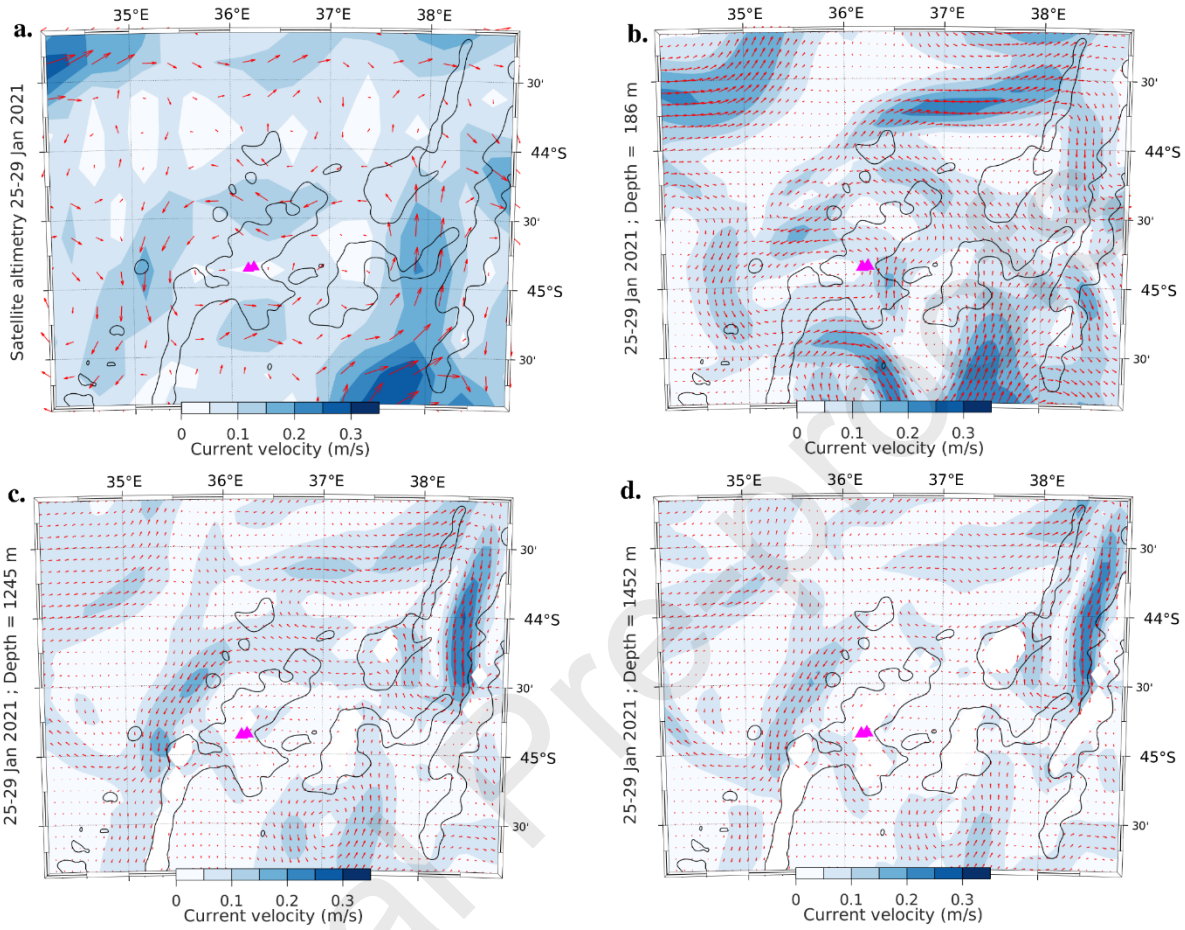

Figure 3. Map of horizontal currents averaged between January 25 and January 29, 2021, from satellite altimetry (a.) and from the GLORYS12 reanalysis at 190 m (b), 1250 m (c) and 1450 m (d). The black line denotes the 2000 m isobath. The location of stations 14 and 15 is indicated by magenta triangles. Units in m s^{-1}.

Focusing on a domain of a few kilometers around the stations, the GLORYS12 currents below 1000 m depth for 28 January 2021 are reported in Fig. 4, together with those measured on station. Two LADCP casts were performed at station 14 (28 January, 17h UTC and 21h UTC) whereas only one was performed for station 15 on 29 January 17h UTC. The two casts at station 14 provide an appreciation of the importance of tidal currents, with nearly opposing directions at a 4h interval. This reversal of currents at station 14 is roughly consistent with the modeled barotropic tidal currents according to TPXO9v5 (green arrows). The principal lunar semidiurnal M2 constituent overwhelmingly dominates, accounting for 99% of the tidal current variance for the period ranging from 27 January to 2 February. The corresponding M2 tidal ellipses are slightly stretched along a southeast-northwest axis (Fig. 4), and identical between station 14 and 15, although the influence of local topography seems to be important as evidenced by the preferential direction of LADCP currents across the saddle point of the ridge, west of station 14. The effective

resolution of the TPXO9 atlas of tidal constituents is 1/6° (>18 km) away from coastal regions while the provided map resolution is 1/30°; therefore, the fine scales of the flow associated with the local bathymetry cannot be resolved. At station 15, the LADCP current below 1000 m depth is northeastward, consistent, albeit larger, with the velocity field from the GLORYS12 simulation, which does not include tides. Note that GLORYS12 currents were nearly constant over the few days preceding *in-situ* measurements. We conclude from this analysis that horizontal currents below 1000 m depth include a substantial contribution from the semidiurnal tide, on the order of 5 cm s^{-1} or more at station 14 where it appears to be the dominant signal. Superimposed on tidal currents, the GLORYS12 simulation features a smaller constant northeastward flow, that seems topographically guided along the ridge. This current is increasingly larger to the east according to GLORYS12 reaching ~ 5 cm s^{-1} at station 15, where its direction is consistent with LADCP data, but also with the slope of isopycnals between stations 14 and 15 (not shown). The differences between LADCP data and model can be explained by many factors, which include, besides tides, the high-frequency/small-scale dynamics that are not resolved.

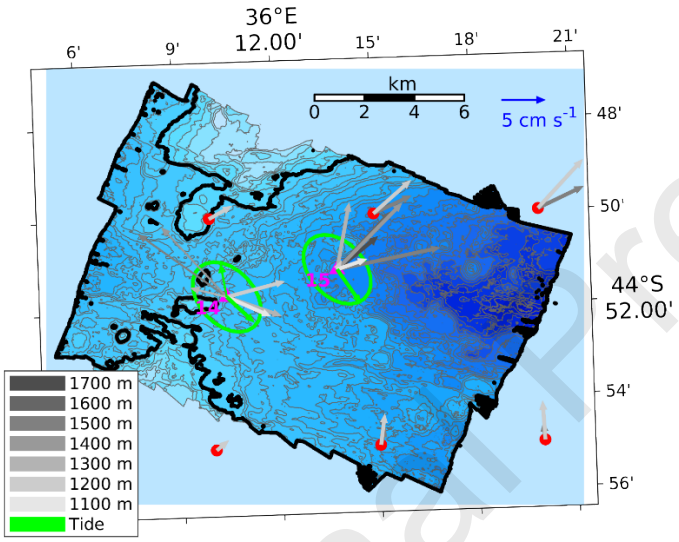

Figure 4. Horizontal currents at depths below 1000 m measured by the LADCP at station 14 on 28 January 2021 and at station 15 on 29 January. A second LADCP cast was performed at station 14 on 28 January, denoted by thin arrows. Green arrows denote the barotropic tidal current at the time of the cast according to the TPXO9v5 model. Corresponding variance ellipses for the dominant M2 constituent computed between 27 January and 2 February are also shown. Current velocity on 28 January from the GLORYS12 reanalysis are shown at a depth of 1250 m and 1450 m (where applicable): red dots denote model grid points. Bathymetry is from the multibeam echo sounder (contour interval 50 m), with the 1250 m isobath highlighted. Unit for the velocity is cm s^{-1} (velocity scale in the top right corner).

3.2. Ra isotopes and ^{227}Ac activities above the SWIR

Table 1: Radium activities at stations 14 and 15, "<DL" indicates activities below detection limit. Here we report i) the Ra activity ratios determined in Mn-cartridges, ii) Ra activities determined using Mn-fibers and iii) Ra activities in seawater determined by combining the ^{226}Ra activities determined using Mn-fibers and the activity ratios determined using Mn-cartridges.

	Activity ratios (Mn-cartridges)						Activities (Mn-fibers)					Activities (seawater)		
Station	Depth (m)	Volume (L)	$^{228}Ra/^{226}Ra$	$^{223}Ra_{ex}/^{226}Ra$	$^{224}Ra_{ex}/^{226}Ra$	$^{224}Ra_{ex}/^{228}Ra$	Depth (m)	Volume (L)	$^{223}Ra_{ex}$ dpm 100L^{-1}	$^{224}Ra_{ex}$ dpm 100L^{-1}	^{226}Ra dpm 100L^{-1}	^{228}Ra dpm 100L^{-1}	$^{223}Ra_{ex}$ dpm 100L^{-1}	$^{224}Ra_{ex}$ dpm 100L^{-1}
14	50	427	0.026 ± 0.007	<DL	0.001 ± 0.0006	0.04 ± 0.02	50	11.9			11.11 ± 0.30	0.29 ± 0.08	<DL	0.01 ± 0.01
	200	601	0.024 ± 0.007	<DL	0.002 ± 0.0006	0.09 ± 0.04	202	12.7			13.17 ± 0.23	0.31 ± 0.09	<DL	0.03 ± 0.01
	900	615	<DL	<DL	<DL	<DL	910	12.7			15.26 ± 0.63	<DL	<DL	<DL
	1000	528	0.009 ± 0.005	0.015 ± 0.0007	<DL	0.02 ± 0.07	1011	11.9			17.27 ± 0.84	0.16 ± 0.08	0.25 ± 0.02	<DL
	1100	548	0.014 ± 0.004	0.021 ± 0.0008	0.003 ± 0.0005	0.22 ± 0.08	1112	11.8			15.48 ± 0.43	0.22 ± 0.07	0.33 ± 0.02	0.05 ± 0.01
	1150	584	0.008 ± 0.004	0.038 ± 0.0012	0.004 ± 0.0004	0.47 ± 0.21	1162	11.9			14.18 ± 0.66	0.12 ± 0.05	0.53 ± 0.03	0.06 ± 0.01
	1200	674	0.010 ± 0.004	0.078 ± 0.0009	0.011 ± 0.0006	1.10 ± 0.44	1213	12.0		0.21 ± 0.16	16.78 ± 0.18	0.16 ± 0.06	1.30 ± 0.02	0.18 ± 0.01
	1250	646	0.014 ± 0.005	0.164 ± 0.0013	0.018 ± 0.0007	1.32 ± 0.44	1265	11.9			15.49 ± 0.32	0.22 ± 0.07	2.54 ± 0.06	0.28 ± 0.01
	1300						1311	11.8			17.74 ± 0.19			
	1340						1353	11.8	3.16 ± 2.21	0.69 ± 0.18	16.63 ± 0.88			
	1360						1370	11.9	1.93 ± 1.84	0.47 ± 0.18	16.01 ± 0.65			
15	700	532	<DL	<DL	<DL	<DL						<DL	<DL	<DL
	1160	579	0.009 ± 0.005	0.009 ± 0.0004	0.001 ± 0.0004	0.16 ± 0.09	1174	11.2		1.05 ± 0.23	15.84 ± 0.36	0.15 ± 0.08	0.14 ± 0.01	0.02 ± 0.01
	1200	503	0.014 ± 0.005	0.005 ± 0.0008	0.002 ± 0.0004	0.16 ± 0.06	1216	11.6		0.37 ± 0.18	16.57 ± 0.34	0.22 ± 0.08	0.09 ± 0.01	0.03 ± 0.01
	1260	665	0.007 ± 0.003	0.010 ± 0.0008	0.010 ± 0.0004	1.48 ± 0.66	1275	11.4			17.51 ± 0.93	0.12 ± 0.05	0.17 ± 0.02	0.18 ± 0.01
	1370	677	0.011 ± 0.005	0.013 ± 0.0011	0.002 ± 0.0004	0.22 ± 0.11	1383	11.3			16.19 ± 0.32	0.17 ± 0.08	0.20 ± 0.02	0.04 ± 0.01
	1500						1519	21.8		0.15 ± 0.10	17.20 ± 0.12			
	1690	630	0.017 ± 0.004	0.296 ± 0.0031	0.049 ± 0.0011	2.91 ± 0.73	1708	11.2	7.05 ± 2.90		17.41 ± 0.31	0.30 ± 0.07	5.15 ± 0.11	0.86 ± 0.02
	1755						1755	11.5	5.28 ± 2.72	0.98 ± 0.20	17.32 ± 0.26			

Table 2: ^{227}Ac activities, in dpm $100L^{-1}$, at stations 14 and 15.

Station	Depth (m)	^{227}Ac (dpm $100L^{-1}$)
14	50	0.023 ± 0.008
	210	0.016 ± 0.006
	900	0.018 ± 0.007
	1000	0.035 ± 0.011
	1100	0.026 ± 0.013
	1160	0.020 ± 0.008
	1200	0.035 ± 0.010
	1260	0.034 ± 0.012
15	700	0.018 ± 0.012
	1160	0.028 ± 0.003
	1200	0.033 ± 0.011
	1260	0.038 ± 0.004
	1370	0.034 ± 0.004
	1690	0.054 ± 0.007

The activities of radium isotopes ($^{223}Ra_{ex}$, $^{224}Ra_{ex}$, ^{226}Ra, ^{228}Ra) are reported in Table 1 and the vertical profiles of $^{223}Ra_{ex}$ and $^{224}Ra_{ex}$ activities are shown in Fig. 5. For both isotopes, we observe very low activities in surface waters at station 14 (< 0.03 disintegration per minuteper 100L; dpm $100L^{-1}$) and activities below the detection limit at 900 m. Activities then increase with increasing depth and reach values up to 0.69 dpm $100L^{-1}$ and 3.16 dpm $100L^{-1}$ at 1353 m for $^{224}Ra_{ex}$ and $^{223}Ra_{ex}$, respectively. Note that both activities slightly decrease after these maxima near bottom depths. A similar vertical distribution is observed at station 15, where higher activities are found below 1200 m. $^{223}Ra_{ex}$ activities reach values of 7.05 dpm $100L^{-1}$ and are higher than the $^{224}Ra_{ex}$ activities (maximum activity of 0.98 dpm $100L^{-1}$) around 1700 m. Short-lived isotopes were even measurable on small volume samples (10.9 - 21.2 L filtered through Mn-fibers), which is uncommon for open ocean waters (Fig.5 and Table 1). Note that the activities of short-lived Ra isotopes determined on Mn-fibers (small volumes) are similar to the activities determined on Mn-cartridges (large volumes), but the uncertainties are much higher on Mn-fibers (Table 1). The Ra activities variability between the two sampling methods may be due to cast-to-cast variability in the plume height, as it was shown in the Mid Atlantic Ridge (Rudnicki et al., 1994) or to the lower sampling resolution of the pump casts. The ^{227}Ac activities determined at stations 14 and 15 are reported in Table 2. The ^{227}Ac activities at station 14 appear to be variable (Fig. 6), with lower activities (~ 0.020 dpm $100L^{-1}$) at the surface, 900 m and 1160 m and relative highest activities (~

0.035 dpm 100L^{-1}) at 1000 m, 1200 m and 1260 m. For station 15, ^{227}Ac activities are in the range of 0.018-0.054 dpm 100L^{-1}, slightly increasing with depth.

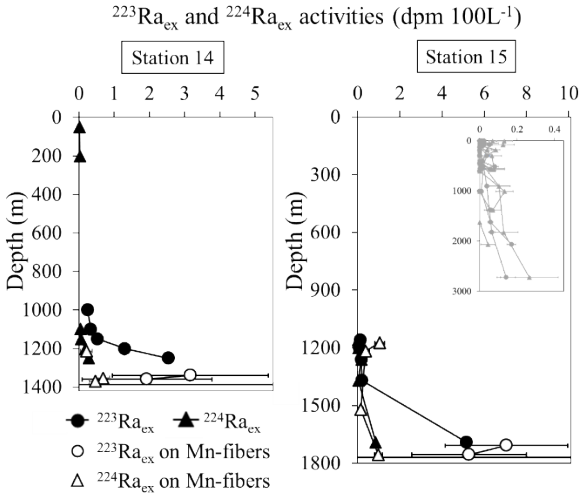

Figure 5. $^{223}Ra_{ex}$ and $^{224}Ra_{ex}$ activities are shown as black circles and black triangles, respectively. Filled symbols represent activities determined by combining the activities determined using Mn-fibers and Mn-cartridges, while open symbols represent activities determined in the Mn-fibers. The graph in the right panel in grey shows, as a comparison, the vertical profiles observed off Kerguelen islands with grey triangle as $^{224}Ra_{ex}$ and grey dots as $^{223}Ra_{ex}$ (Sanial et al., 2015). Errors bars are reported but are often within the symbol. The horizontal lines represent the depth of the seafloor.

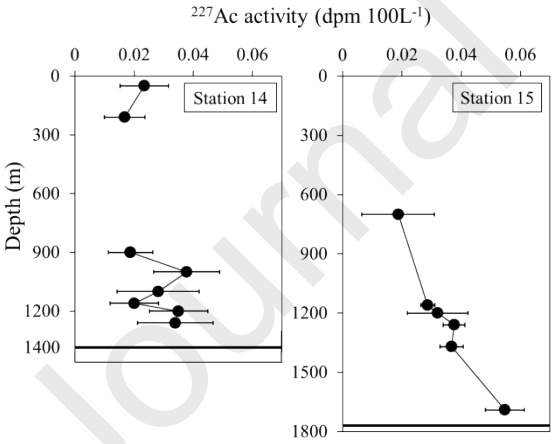

Figure 6. ^{227}Ac activities are shown as black circles. The horizontal lines represent the depth of the seafloor.

The vertical profiles of ^{226}Ra and ^{228}Ra are shown in Fig. 7. ^{228}Ra activities are up to 0.31 dpm 100L^{-1} in surface waters at station 14 but are below the detection limit at intermediate depths (700 m and 900 m at stations 14 and 15, respectively). Deeper, ^{228}Ra activities become detectable again, increasing with depth compared to intermediate waters and reach values of 0.25 dpm 100L^{-1} near the seafloor at both stations. ^{226}Ra activities range from 11.1 dpm 100L^{-1} in surface waters at

station 14 to activities superior to 17 dpm 100L^{-1} in the deep waters of station 15. Note that the ^{226}Ra activities in deep waters (below 1200 m) appear to be more variable at station 14.

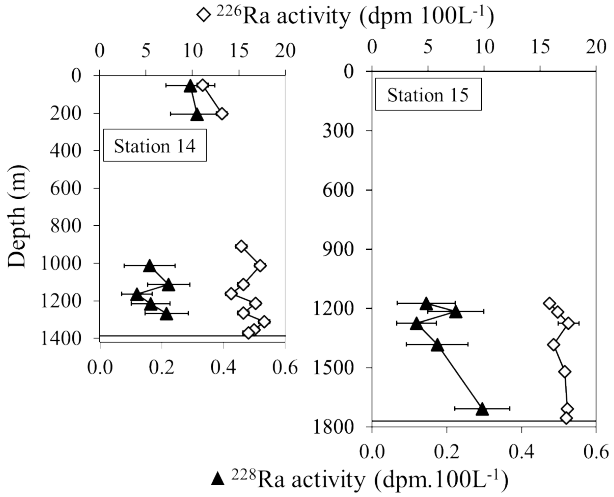

Figure 7. ^{226}Ra and ^{228}Ra activities are shown as white diamonds and black triangles, respectively. The horizontal lines represent the depth of the seafloor. Errors bars for ^{226}Ra are reported but are often within the symbol.

4 Discussion

4.1 Ra isotopes and ^{227}Ac activities above the SWIR

Far from any continental source, the activities of the short-lived radium isotopes rapidly decrease due to radioactive decay and mixing. The ^{223}Ra and ^{224}Ra activities in the open ocean are therefore often negligible, with the exception of waters located near the seafloor that are slightly enriched in ^{223}Ra and ^{224}Ra, as a consequence of Ra diffusion from deep-sea sediments (GEOTRACES Intermediate Data Product Group, 2021). The $^{223}Ra_{ex}$ and $^{224}Ra_{ex}$ activities reported near the seafloor at stations 14 and 15 display maximum values of 7.05 dpm 100L^{-1} and 0.98 dpm 100L^{-1}, respectively. These activities clearly exceed the activities usually found in open ocean waters (GEOTRACES Intermediate Data Product Group, 2021). As a comparison, we report in Fig. 5 all the vertical profiles of $^{223}Ra_{ex}$ and $^{224}Ra_{ex}$ determined off Kerguelen Islands in the Southern Ocean (Sanial et al., 2015). Although the waters offshore Kerguelen are slightly impacted by the islands and at depth by the input from the sediments, the $^{223}Ra_{ex}$ and $^{224}Ra_{ex}$ never exceed 0.3 dpm 100L^{-1} for both isotopes. At both stations 14 and 15, the $^{223}Ra_{ex}$ and $^{224}Ra_{ex}$ activities are very low above 900 m in agreement with the general pattern described above. At station 14, the highest $^{223}Ra_{ex}$ and $^{224}Ra_{ex}$ activities are observed at 1350 m depth, about 35 m above the seafloor while at station 15, the maximum $^{223}Ra_{ex}$ activity is observed at 1700 m depth, about 60 m above the seafloor. As a comparison, Charette et al. (2015) reported maximum activities of 0.97 dpm 100L^{-1} for $^{223}Ra_{ex}$ while never exceeding 0.16 dpm 100L^{-1} for $^{224}Ra_{ex}$, in the deepest samples located ~ 80 m above the ridge crest in the TAG neutrally buoyant plume in the Mid-Atlantic Ridge. Note that all these latter activities are considerably lower than those reported here. As another comparison, Neuholz et al (2020a) reported $^{223}Ra_{ex}$ activities up to 0.11 dpm 100L^{-1} and up to 1.4 dpm 100L^{-1} for $^{224}Ra_{ex}$ in the Kermadec arc. The especially high $^{223}Ra_{ex}$ and $^{224}Ra_{ex}$

activities reported near the seafloor at these two stations cannot be explained by diffusion from bottom sediments. Considering the rocks observed in the area (e.g., lava pillows) by Humler et al. (2001) and the geomorphological features (volcano shape) detected during the bathymetry survey (Fig. 1), volcanism could be invoked as a source term. However, the different surveys conducted in the area (Humler et al., 2001; Sato et al., 2013; this study) did not find any evidence for *active* volcanism in the area. Hydrothermal activity (circulation of fluid into the basalts) is the most likely candidate to explain the Ra signature reported here.

In contrast, the ^{227}Ac activities, up to 0.055 dpm 100L^{-1}, are close to the ^{227}Ac usually observed in open ocean waters outside the influence of hydrothermal vents. A similar pattern was observed in other studies conducted in the vicinity of low temperature ridges, where large increases in $^{223}Ra_{ex}$ and $^{224}Ra_{ex}$ activities were not accompanied by an increase in ^{227}Ac activities (Moore et al., 2008; Geibert et al., 2008). As a comparison, Moore et al. (2008) reported in the Puna ridge activities up to 1.9 dpm 100L^{-1} for $^{223}Ra_{ex}$, and up to 0.4 dpm 100L^{-1} for $^{224}Ra_{ex}$ while the ^{227}Ac activities never exceeded 0.02 dpm 100L^{-1} (Geibert et al., 2008). This is in contrast with Kipp et al. (2015) who reported significant enrichment of ^{227}Ac within the neutrally buoyant hydrothermal plume overlying the TAG vent field.

The ^{226}Ra activities reported here are in the typical range of activities usually observed in Southern Ocean waters (i.e. 15 to 17.7 dpm 100L^{-1}) (Charette et al., 2007; Chung, 1987; Ku and Lin, 1976; van Beek et al., 2008). However, while typical open ocean profiles display a smooth increase in the ^{226}Ra activities with increasing depth (Charette et al., 2007; Chung, 1987; Ku and Lin, 1976; van Beek et al., 2008), we observe a significant variability in the ^{226}Ra activities (Fig. 7). This is especially true at station 14 between 910 m and the bottom and to a lesser extent at station 15 where a small peak is found at 1275 m. These patterns may be related to the presence of a nearby hydrothermal activity, although ^{226}Ra may not be as strongly conclusive as the short-lived Ra isotopes. It cannot be excluded that the high ambient ^{226}Ra activities of the Southern Ocean waters would prevent any excess ^{226}Ra supplied from the ridge to be discerned.

In contrast to ^{226}Ra, the ^{228}Ra activities in the Southern Ocean are extremely low (< 0.15 dpm 100L^{-1}; van Beek et al., 2008; Sanial et al., 2015; Inoue et al., 2022) and are therefore more sensitive to an input from any source term. This is often the case in surface waters in the vicinity of continents/islands and near the seafloor where slight increases are detected (Charette et al., 2007; van Beek et al., 2008; Sanial et al., 2014). The mid water column is often depleted in ^{228}Ra relative to surface and deep waters due to slow downward and upward vertical mixing for these two sources (Charette et al., 2007). At both stations 14 and 15, the ^{228}Ra activities clearly increase with depth from below the detection limit (700-900 m) to ca. 0.2-0.3 dpm 100 L^{-1} near bottom sediments. Such activities, however, are still in the range of activities reported in the Southern Ocean near bottom sediments (see e.g., van Beek et al., 2008; Sanial et al., 2015).

In summary, there is a clear unusually high signature of short-lived Ra isotopes near the seafloor, with the $^{223}Ra_{ex}$ activities (up to 7.05 dpm 100 L^{-1}) being higher than the $^{224}Ra_{ex}$ activities (up to 0.98 dpm 100 L^{-1}). The patterns of ^{226}Ra, ^{228}Ra and ^{227}Ac activities are less conclusive. We will thus investigate in the following sections the different processes that could lead to the patterns observed among the different isotopes determined in the vicinity of a hydrothermal source.

4.2 Processes at play in the vicinity of the hydrothermal vents as indicated by $^{224}Ra_{ex}/^{228}Ra$, $^{223}Ra_{ex}/^{226}Ra$ and $^{224}Ra_{ex}/^{223}Ra$ ratios

Owing to the different half-lives of the Ra isotopes, the fluid circulating in the crust may not be similarly enriched in all Ra isotopes. Due to their shorter half-lives, ^{223}Ra and ^{224}Ra are regenerated faster than ^{226}Ra and ^{228}Ra (Charette et al., 2007; Garcia-Orellana et al., 2021; Fig. 8). Because circulation of seawater through the crust occurs generally over relatively short time scales, from days to a few years (Kadko and Moore, 1988; Kadko et al., 2007), Ra may be frequently flushed from the system. As the production of Ra isotopes is notably governed by their half-lives, the residence time of seawater within the crust may not allow a significant ingrowth of the long-lived Ra isotopes by radioactive decay of their parents. Thus, unless the main input process is due to weathering and dissolution of radium rich phases (Hammond et al., 1988), the circulated fluid is expected to display $^{223}Ra_{ex}/^{226}Ra$ and $^{224}Ra_{ex}/^{228}Ra$ activity ratios higher than the rock ratio.The $^{224}Ra_{ex}/^{228}Ra$ activity ratios can also be affected by the residence time of seawater into the crust depending on the type of the hydrothermal vent. Neuholz et al. (2020a) suggest that the fluid migration is relatively slow for diffuse fluids (as in ultramafic systems) and likely faster for focused venting fluids (as in volcanic systems). Similarly, Kipp et al. (2018) have observed that the $^{224}Ra_{ex}/^{228}Ra$ activity ratio is generally close to 1 in high temperature fluids, suggesting that the residence time of fluids in the crust is long enough (on the order of years) to allow these isotopes to reach secular equilibrium. In contrast, they observe $^{224}Ra_{ex}/^{228}Ra$ activity ratio often higher (up to 5.5) in low temperature hydrothermal fluids. Several processes discussed by Kipp et al. (2018) may explain the $^{224}Ra_{ex}/^{228}Ra$ activity ratios >1. One of them is the faster regeneration of short-lived Ra isotopes compared to long-lived Ra isotopes, as explained above. The $^{224}Ra_{ex}/^{228}Ra$ activity ratios can also be affected by the residence time of seawater into the crust depending on the type of the hydrothermal vent. Neuholz et al. (2020a) suggest that the fluid migration is relatively slow for diffuse fluids (as in ultramafic systems) and likely a faster for on focused venting fluids (as in volcanic systems). Alternatively, there may be a greater sorption of ^{228}Th at the end of the flow path, with the result that the circulating fluid would become enriched in ^{224}Ra. This hypothesis seems unlikely due to the high particle affinity of ^{228}Th. Finally, significant sorption or precipitation of long-lived Ra isotopes - including via $BaSO_4$ co-precipitation - and efficient ^{224}Ra recoil would also increase the $^{224}Ra_{ex}/^{228}Ra$ ratio in the fluid. Because the sorption process is slow compared to the decay of ^{223}Ra and ^{224}Ra, it is unlikely that short-lived Ra isotopes would be removed by sorption before decay. The $^{224}Ra_{ex}/^{228}Ra$ and $^{223}Ra_{ex}/^{226}Ra$ ratios will also decrease when the plume is transported away from the source, because radioactive decay of ^{224}Ra and ^{223}Ra is faster than ^{228}Ra and ^{226}Ra. Therefore, the $^{224}Ra_{ex}/^{228}Ra$ ratio in the plume may be indicative of the residence time of the fluid in the crust, which may be related to the fluid temperature and/or the age of the plume.

Assuming that stations 14 and 15 are located in the near vicinity of the vents, the $^{224}Ra_{ex}/^{228}Ra$ and $^{223}Ra_{ex}/^{226}Ra$ ratios may be compared to the ratios reported in hydrothermal fluids (Kipp et al., 2018), keeping in mind that these ratios decrease with increasing distance from the source. In samples displaying the highest $^{223}Ra_{ex}$ and $^{224}Ra_{ex}$ activities, we observe $^{224}Ra_{ex}/^{228}Ra$ activity ratios of 3.46 at 1690 m (station 15), 1.32 at 1250 m (station 14) and 1.10 at 1200 m

(station 14). An explanation that would reconcile these different ratios would be that i) the high ratio observed at station 15 may be indicative of a plume resulting from a low temperature fluid (such type of fluid exhibiting ratios up to 5.5; Kipp et al., 2018) and ii) the slightly lower ratios reported at station 14 may thus result from the decrease of the $^{224}Ra_{ex}/^{228}Ra$ ratio when being transported away from the source. This does not mean that both stations are under the influence of the same source. There could be multiple sites of hydrothermal discharge in the region.

The distinction between low and high temperature fluids is not as clear when looking at the $^{223}Ra_{ex}/^{226}Ra$ activity ratios. In the data reported here, a $^{223}Ra_{ex}/^{226}Ra$ activity ratio up to 0.16 is observed in the deep water at station 14 and up to 0.3 in the deep water at station 15. This latter value is comparable to data observed at Baby Bare Seamount and is significantly higher (about one order of magnitude) than values usually observed in other vent fluids (i.e., 0.044-0.073; Kipp et al., 2018). The ^{223}Ra enrichment of the circulating fluid may be explained by the particle reactive behavior of Ac - compared with Ra - that will adsorb onto mineral surfaces (Moore et al., 2008; Kipp et al., 2015). With time, ^{223}Ra will be produced by the decay of ^{227}Ac and will partition into the aqueous phase. The seawater entering into the ridge also contains ^{232}Th, the parent of ^{224}Ra, that is deposited onto the surfaces, but in much lower concentrations than ^{231}Pa, the parent nuclide of ^{227}Ac and ^{223}Ra (Fig. 8). The expected activity ratio of dissolved $^{232}Th/^{231}Pa$ in Southern Ocean waters is on the order of 0.2-0.3 (calculated from Chase et al., 2003 and Thomas et al., 2006). The production of ^{224}Ra is thus relatively low compared to ^{223}Ra production. This may also explain the

low $^{224}Ra_{ex}/^{223}Ra_{ex}$ ratios observed above the SWIR. Similar phenomena have been observed in low temperature hydrothermal vents (Moore et al., 2008; Kipp et al., 2015).

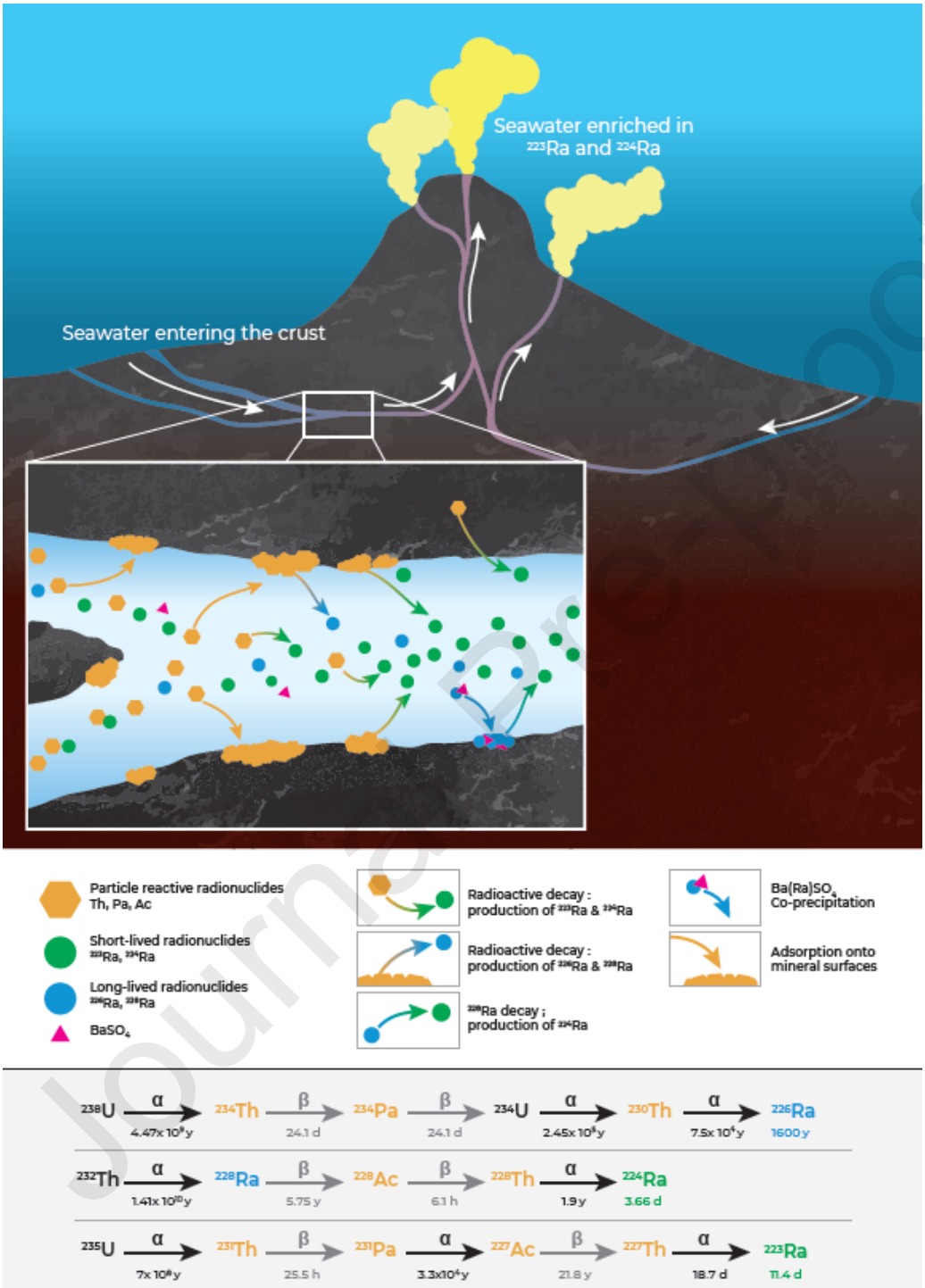

Figure 8. Conceptual figure illustrating the circulation of the fluid within a hydrothermal system and the associated partitioning of radionuclides from the U-Th decay chain.

4.3. Determination of vertical mixing using Ra isotopes

The vertical profiles of Ra isotopes can be used to estimate a vertical eddy diffusivity coefficient (K_Z) (Li et al., 1980; Moore, 1972; Sarmiento et al., 1982; Ku and Luo, 1994; Charette et al., 2007; van Beek et al., 2008). The short half-lives of ^{223}Ra and ^{224}Ra probably make them less sensitive to lateral advection than other radionuclides (e.g., ^{227}Ac, ^{228}Ra and ^{226}Ra) which display longer half-lives. Moreover, the vertical profiles of ^{227}Ac, ^{228}Ra and ^{226}Ra may be more inclined to be impacted by other sources due to their longer half-life. Assuming (1) steady state on the time scale of ^{223}Ra and ^{224}Ra half-lives (i.e., the supply of ^{223}Ra and ^{224}Ra balances Ra loss by radioactive decay and mixing), (2) no addition or loss of Ra except for radioactive decay and (3) that the vertical dispersion of radium can be approximated to a diffusive process (rather than advective), then a 1D model can be written as follows:

$$\frac{dA}{dt} = K_z \frac{\partial}{\partial Z}\left(\frac{\partial A}{\partial Z}\right) - \lambda A = 0 \qquad (1)$$

, where K_Z is the vertical eddy diffusivity coefficient, A is the Ra activity, z is the depth above the bottom and λ is the Ra decay constant. The use of a 1D model can be further justified by the structure of horizontal currents below 1000 m (Section 3.1), which are not only small, but more importantly fairly constant with depth (i.e., barotropic).

The solution of the equation (1) is given by:

$$A_z = A_0 \times exp(-z \times \sqrt{\frac{\lambda}{K_z}}) \qquad (2)$$

, where $A=A_0$ at z=0 (bottom depth) and A=0 at $z\rightarrow\infty$. We applied the equation 2 to the vertical profiles of $^{223}Ra_{ex}$ and $^{224}Ra_{ex}$ obtained on Mn-cartridges at station 14 between 1000 m and 1250 m. K_Z can be calculated from the best exponential fit coefficient of a plot of $^{223}Ra_{ex}$ or $^{224}Ra_{ex}$ vs distance from bottom, by determining the coefficient $m = (\lambda/K_Z)^{-2}$. We have chosen here not to include the activities of short-lived Ra isotopes determined on Mn-fibers in the K_Z calculation due to their large associated error bars.

Fig. 9 shows the fit of the model to the $^{223}Ra_{ex}$ and $^{224}Ra_{ex}$ vertical profiles. We obtain K_Z of 38 ± 2 cm² s^{-1} (m = -0.01365 ± 0.00045; r = 0.999; n = 5) derived from $^{223}Ra_{ex}$ and 149 ± 43 cm² s^{-1} (m = -0.01213 ± 0.00249; r = 0.962; n = 4) derived from $^{224}Ra_{ex}$. These K_Z values are higher than those previously reported on the Crozet or Kerguelen shelves by Charette et al. (2007) and van Beek et al. (2008), respectively (K_Z = 1.5 cm² s^{-1} in both shelves at similar depths), and two or three orders of magnitude higher than the K_Z estimated by Law et al. (2003) in the open Southern Ocean (K_Z = 0.11 ± 0.2 cm² s^{-1}). However, in general, rough topography at oceanic ridges leads to strong mixing compared to the ocean interior (Walter et al. 2010). For example, over the SWIR, MacKinnon et al. (2008) reported K_Z higher than 100 cm² s^{-1} near the seafloor in Atlantis II Fracture zone. High diffusivity coefficients are also observed in the vicinity of hydrothermal

systems. Neuholz et al. (2020a) thus estimated K_Z of 2000 cm² s^{-1} in the rise height of a plume in the Kermadec arc, while diffusivity coefficients of 130 and 300 cm² s^{-1} were observed at Rainbow and Lucky Strike sites (Thurnherr et al., 2022; St Laurent and Thurnherr, 2007). As another comparison, vertical diffusivity coefficients between 40 and 800 cm² s^{-1} were estimated in the Mid-Atlantic Ridge region (Keir et al., 2008; Walter et al., 2010). The relatively high K_Z values reported here highlight the strong vertical mixing on the ridge flank region. Interestingly, Walter et al. (2010) suggest that slow spreading ridges, because they are characterized by a steeper, more rugged bathymetry, favor an enhanced level of internal wave generation from currents interacting with the topography influencing the strength of the mixing of the plume.

Nevertheless, here we observe a significant difference between the K_Z values determined using the two different Ra isotopes, with K_Z (^{224}Ra) > K_Z (^{223}Ra). This trend has been invariably observed in studies reporting estimates of horizontal or vertical diffusivity coefficients (Moore, 2000a; Hancock et al., 2006; Charette et al., 2007; Colbert and Hammond, 2007; Lamontagne et al., 2008; Moore and de Oliveira, 2008; Koch-Larrouy et al., 2015) and several hypotheses have been proposed to explain this difference. First, the K_Z calculation is based on the assumption that it is constant over the distance studied, although it may vary within the water column. Second, the K_Z values are derived from two isotopes displaying different half-lives. The K_Z thus obtained reflects an integrated pattern related to the residence time of the radionuclide in the water column. The lower K_Z estimates derived from $^{223}Ra_{ex}$ may thus be explained by a longer-term integration of the signal (space, time) compared to the K_Z estimated from $^{224}Ra_{ex}$ vertical profiles. In addition, short fluctuations in end-member concentrations or water column residence time over short periods of time may impact these calculations, especially for $^{224}Ra_{ex}$. Finally, Stachelhaus and Moran (2012) suggest that this difference could be attributed to differential or scale-dependent diffusion. In the present study, we thus have no reason to choose one K_Z value over the other (i.e., derived from $^{223}Ra_{ex}$ or from $^{224}Ra_{ex}$).

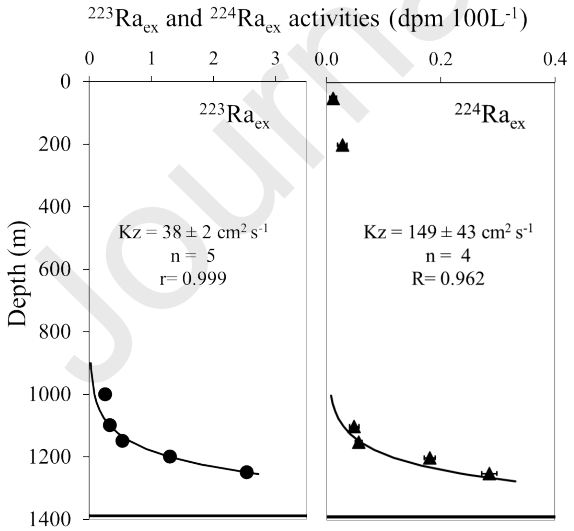

Figure 9. Vertical eddy diffusivity coefficient (K_Z) estimation at station 14 using a simple one-dimensional diffusion model applied to the vertical profiles of $^{223}Ra_{ex}$ (left panel) and $^{224}Ra_{ex}$ (right

panel). The best exponential fits considering Ra data in the 1000–1250 m depth interval together with the R value are reported. The horizontal lines represent the depth of the seafloor. The uncertainties on the K_Z are derived from the uncertainty on the best exponential fit coefficient of Ra activities as function of distance from bottom (Equation 2).

4.4 Vertical flux of dissolved Fe in the water column

Very few studies reported quantification of chemical fluxes - including dissolved Fe - associated with hydrothermal vents. Recently, Neuholz et al. (2020b) quantified the Fe and Mn fluxes associated with submarine hydrothermal discharge (so called, SHD) at Brother volcano in the southern Kermadec arc (Pacific Ocean) based on the approach developed to quantify chemical fluxes associated with submarine groundwater discharge (SGD). This method is based on building the Ra inventory in the plume and requires knowledge of the volume and residence time of the plume, as well as the chemical concentrations in the fluid (endmember), including Ra and chemical concentrations. This latter information can only be obtained when a full study is conducted, presumably at a site where the presence and location of hydrothermal vents have been already identified by previous studies. Since the present study was an exploratory study, we do not have the detailed view on the volume of the plume and on the endmember concentrations, as is required by the method of Neuholz et al. (2020b). Here, we attempt to provide an estimate of the dFe flux by using a method that was applied to quantify the vertical chemical fluxes in open ocean waters that are not impacted by hydrothermal vents. The method combines the vertical eddy diffusivity coefficients K_Z estimated from the vertical profiles of Ra isotopes with the vertical gradient of dFe. Charette et al., (2007) and van Beek et al. (2008) thus quantified the vertical fluxes of dFe associated with the Crozet and Kerguelen deep-sea sediments. We used the same method using the K_Z values determined from the $^{223}Ra_{ex}$ and $^{224}Ra_{ex}$ vertical profiles and the vertical gradient of dFe (data from Baudet et al., submitted). As no dFe was sampled at station 15, the flux of dFe was only determined at station 14. The vertical gradient of dFe was found to be $4.28\ 10^{-4} \pm 0.2.36\ 10^{-4}$ nmol $L^{-1}\ m^{-1}$ ($r = 0.44$; $n = 16$). The sharp peak of dFe at 1300 m was not considered in the calculation (flagged as an outlier by Baudet et al., submitted). By multiplying the K_Z values by the dFe gradient between 975 m and 1364 m depth, the vertical fluxes of dFe thus obtained are 139 ± 77 nmol $m^{-2}\ d^{-1}$ and 552 ± 344 nmol $m^{-2}\ d^{-1}$, considering the K_Z values determined from $^{223}Ra_{ex}$ and $^{224}Ra_{ex}$, respectively. Errors on the dFe fluxes results from the propagation of the uncertainties associated with the K_Z and the vertical gradient of dFe. This flux is even higher if we consider a larger depth interval (between 700 m and the bottom) to calculate the dFe vertical gradient. A value of $9.11\ 10^{-4} \pm 0.1.07\ 10^{-4}$ nmol $L^{-1}\ m^{-1}$ ($r = 0.90$; $n = 19$) is then obtained for the dFe gradient, which is slightly higher than the value calculated above. The resulting vertical flux of dFe is thus 297 ± 38 nmol $m^{-2}\ d^{-1}$ considering the K_Z derived from $^{223}Ra_{ex}$ and 1173 ± 367 nmol $m^{-2}\ d^{-1}$, considering the K_Z derived from $^{224}Ra_{ex}$. Overall, the dFe vertical fluxes calculated here range from 139 to 297 nmol $m^{-2}\ d^{-1}$ as derived from $^{223}Ra_{ex}$ and from 552 to 1173 nmol $m^{-2}\ d^{-1}$ as derived from $^{224}Ra_{ex}$.

Schine et al. (2021) estimated dFe fluxes of possible hydrothermal origin ranging from 440 up to 530 nmol $m^{-2}\ d^{-1}$ in the Pacific Southern Ocean, which is consistent with our estimates. Other studies reported dFe fluxes associated with similar systems, with, however, different units which complicates the comparison with our estimates. **Neuholz et al. (2020) thus estimated dFe fluxes in the Brothers volcanoes ranging from 0.15 mol s^{-1} to 71.2 mol s^{-1} while other studies in Juan de Fuca, Rainbow vent field or again Northern Mariana Islands, reported dFe fluxes of 0.61 mol s^{-1}, 9.6 mol s^{-1} and 0.14 mol s^{-1}, respectively (German et al., 2010; Massoth et al., 1994;**

Buck et al., 2018). Using a geochemical model, Resing et al. (2015), estimated a global hydrothermal Fe flux of 4 ± 1 Gmol yr^{-1} while Roshan et al. (2020) estimated a much lower Fe flux of about 0.12 ± 0.07 Gmol yr^{-1} taking into account particulate-dissolved Fe exchange. The dFe fluxes estimated in this study are much higher than those previously observed on the Kerguelen Plateau outside any influence of a hydrothermal activity by van Beek et al. (2008) using ^{228}Ra data (1.0-14.3 nmol m^{-2} d^{-1}), by Blain et al. (2007) (31 nmol m^{-2} d^{-1}), or again by Tagliabue et al. (2014) where the authors estimate a vertical diffusive dFe flux range of 0.0016-0.0157 µmol m^{-2} d^{-1} for the Southern Ocean. On the Crozet Plateau, also outside any influence of a hydrothermal activity, Charette et al. (2007) estimated a vertical dFe flux up to 61 nmol m^{-2} d^{-1}, which is considerably lower than the one determined here. Finally, we note that the vertical dFe flux reported in this study is in the same order of magnitude as the horizontal (390 nmol m^{-2} d^{-1}) or atmospheric (100 nmol m^{-2} d^{-1}) fluxes estimated by Planquette et al. (2007) in the Crozet region. The results presented here confirm that hydrothermal systems are a significant source for dFe into the deep ocean. When combined to a strong vertical mixing, significant fluxes of dFe may be transported towards shallower waters. If this dFe reaches surface waters, it could stimulate phytoplankton blooms as suggested by Tagliabue et al. (2010), Ardyna et al. (2019) or Schine et al. (2021). If this study clearly highlights a high vertical flux of dFe at depth (below 700 m), it cannot be concluded here that dFe reaches the upper water column and contributes to fuel phytoplankton bloom.

4.5. Uncertainties around the Ra-based dFe flux estimation

Radium isotopes (with the exception of ^{226}Ra) are generally present in very low concentrations in the open ocean, necessitating the sampling of large volumes of seawater (several hundred liters) in order to measure these activities. The errors associated with $^{223}Ra_{ex}$ and $^{224}Ra_{ex}$ measurements are commonly estimated by an error propagation method (Garcia-Solsona et al. 2008), leading to errors of the order of 30 to 40 % (up to 53% for the measurement of $^{224}Ra_{ex}$ in this study). Note that the relative low errors associated with the ^{223}Ra activities compared to others studies (up to 14.5 % in this study) are due to i) the relatively high ^{223}Ra activities, ii) the large volumes that we collected and iii) the repeated measurements (3 to 5 times) that allowed us to reduce the uncertainty on the ^{227}Ac activity and thus on the ^{223}Ra activities determined using RaDeCC (Le Roy et al., 2017; Léon et al., submitted). The uncertainty associated with the K_Z value derives from the uncertainty on the m coefficient determined from the best exponential fit of the ^{223}Ra and ^{224}Ra vertical profiles. The relative standard errors (RSD) associated with the K_Z values are thus between 5 and 30 %, when using the vertical profiles of ^{223}Ra and ^{224}Ra, respectively. Finally, the uncertainty on the dFe flux is determined by propagating the uncertainty on the K_Z (Fig. 9) and the uncertainty on the vertical dFe gradient. As the dFe gradient has RSD of 12-55 % depending on the depth interval that is considered, the dFe fluxes display RSD of 13 to 62 %. Here, we prefer to report a range of dFe fluxes, the high and low values of the range being determined using the K_Z values determined using either $^{223}Ra_{ex}$ or $^{224}Ra_{ex}$. The range of fluxes are far greater than represented by the measurement inaccuracy described above.

In addition to the mathematical error associated with the estimate of the different parameters that are described above, sources of uncertainty may also come from the assumptions around these estimates (steady state assumption on the time scale of ^{223}Ra and ^{224}Ra half-lives, no addition or loss of Ra except for radioactive decay and vertical dispersion of radium can be approximated to a diffusive process, rather than advective). We cannot state with certainty that the

system is at steady state on the time scale of ^{223}Ra and ^{224}Ra half-lives. Despite their short half-lives, it is possible that the source releases these isotopes variably over time. Moreover, the tidal influence of the currents can also cause Ra concentrations to vary along the water column. The vertical profiles of ^{223}Ra and ^{224}Ra activities may be affected by additional inputs - other than from the hydrothermal activity - following the radioactive decay of dissolved or particulate ^{227}Ac or ^{228}Th. This includes Ra that diffuses out of the sediment or Ra that may be released from bottom nepheloid layers that would constitute an additional benthic Ra source, especially for ^{223}Ra which has a longer half-life (Kipp et al., 2015, Neuholz et al. 2020a). However, no increase in turbidity near the bottom was noticed, suggesting the absence of suspended particles in bottom layers. In addition, the minor enrichments from the bottom of ^{227}Ac and ^{228}Th (not shown here) probably do not release a significant amount of ^{223}Ra or ^{224}Ra and are considered to add minor uncertainties on the $^{223}Ra_{ex}$ or $^{224}Ra_{ex}$ estimates. The high $^{223}Ra_{ex}$ and $^{224}Ra_{ex}$ activities observed at depth are thus likely not significantly impacted by any other source that is presumably minor as a comparison to the hydrothermal input. Alternatively, in hydrothermal plumes, Ra can potentially adsorb onto the surfaces of manganese oxides or be incorporated into barite ($BaSO_4$) and then be partially removed near the source (Moore and Reid, 1973; Reid et al., 1979), a process that may impact the Ra vertical profiles. Finally, significant variability of the plume dispersion even at small space and time scales (Ardyna et al., 2019) may be expected. This suggests that the values of K_Z and dFe fluxes estimated here are likely to be valid only for that position at the time when the samples were taken.

In summary, taking into account all the uncertainties mentioned above and considering the large uncertainties associated with K_Z and dFe fluxes, these vertical fluxes must be considered as an approximate order of magnitude, limited in space and time. Still, this information is valuable, since information on the chemical fluxes associated with these systems are scarce. The difficulties to generate accurate fluxes of trace elements based on the Ra approach in hydrothermal deep-sea environment has already been demonstrated by Neuholz et al. (2020a,b). For further investigations in this region, a more detailed study is needed, including the study of the plume at a higher spatial resolution (additional stations), which should allow us to better locate both the source and the plume pathways and to better constrain the geochemical processes involved in these systems.

4.6. Speculation on the location of the source

Both the short half-lives and the high activities of $^{224}Ra_{ex}$ and $^{223}Ra_{ex}$ determined at stations 14 and 15 suggest that these stations are located in the near vicinity of the source term. These vertical profiles, however, only provide a 1D view of the water column. By using physical data, we attempt to have a more complete view of the dynamics in the region, which is important to consider since the currents transport the plume away from the source. We aim to use these physical data to estimate how far a signal released at the bottom may be transported away from the source and potentially also to help locating the source term. The analysis of the horizontal circulation below 1000 m presented in Section 3.1 indicates a substantial contribution from tidal currents, a dominant signal at station 14, with a constant northeastward flow guided by the ridge superimposed, larger at station 15 where it reaches ~ 5 cm s^{-1} according to the model (Fig. 4). The periodic nature of tidal currents will tend to disperse the different radionuclides more efficiently if these currents are spatially variable. Here the fairly isotropic and homogeneous nature of modeled tidal ellipses (Fig. 4) suggests that barotropic tidal currents will predominantly displace the different chemical elements around in a periodic movement, although we recognize that the tidal model is too coarse to accurately account for the variability of the flow at the short spatial scales

of the local bathymetry. The background mean flow, on the other hand, consistently advects the different radionuclides with a mean flow of 5 cm s^{-1}. A mean flow of 5 cm s^{-1} translates to 4.3 km day^{-1}, that is a distance of ~30 km over one week, assuming that such high Ra signature can persist over such time scale, which is already a high estimate. The source term(s) is(are) thus expected to be within 30 km distance from these stations.

Note that we observe a decrease in the $^{224}Ra_{ex}/^{228}Ra$ activity ratios between the two stations at a potential density of about 27.4 (corresponding to 1200 and 1250 m depth for station 14 and at 1160 and 1200 m depth for station 15) with activity ratio decreasing from 1.21 at station 14 to 0.19 at station 15. Assuming that stations 14 and 15 are impacted by the same source and considering an eastward-northeastward transport (i.e., from station 14 to station 15; see section 3.1 and Figures 3 and 4), we thus estimate a transit time of about 10 days, yielding to a transport rate of 0.5 cm s^{-1}. A mean flow of 0.5 cm s^{-1} translates to 0.4 km day^{-1}, that is a distance of ~3 km over one week. The latter estimate determined using a reduced transport rate (0.5 cm s^{-1}) suggests that the source term may be located even closer (within 3 km) to the investigated stations than when using the transport rate reported above (5 cm s^{-1}).

A more precise determination of the source position, however, would require to know the Ra activities (and activity ratios) at the source term and to have a more detailed view of the Ra distribution in the region, in case the plume cannot be traced with temperature and suspended particles.

5 Conclusion

These new investigations around the fracture above the SWIR have led to the establishment of a very high-resolution bathymetric map of this area. While there was no clear signature on the vertical profiles of temperature, dissolved oxygen, beam transmission or salinity, ^{223}Ra and ^{224}Ra activities reported in this area highlight the presence of a hydrothermal system, likely located in the near vicinity of the investigated stations due to the short half-lives of these radionuclides. The high activities of $^{223}Ra_{ex}$ and $^{224}Ra_{ex}$ compared to long-lived Ra isotopes could be explained by a faster regeneration rate of these isotopes during seawater circulation within the crust. Moreover, we reported here among the highest $^{223}Ra_{ex}$ activities observed in the vicinity of hydrothermal systems, unaccompanied by its parent, ^{227}Ac. This result suggests that ^{227}Ac is adsorbed onto mineral surfaces during seawater circulation within the crust whereas $^{223}Ra_{ex}$ is likely released into the dissolved phase. The high $^{224}Ra_{ex}/^{228}Ra$ ratios reported here are in favor of a low temperature fluid. We estimated vertical diffusivity coefficients K_Z of 38 - 149 $cm^2\ s^{-1}$ using the vertical profiles of $^{223}Ra_{ex}$ and $^{224}Ra_{ex}$ activities, respectively. By combining these coefficients to the vertical gradient of dFe, we estimated dFe vertical fluxes of 139 - 297 $nmol.m^{-2}.d^{-1}$, as derived from $^{223}Ra_{ex}$ activities and of 552 – 1173 $nmol.m^{-2}.d^{-1}$, as derived from $^{224}Ra_{ex}$ activities. These estimates highlight a strong vertical mixing on the flanks of the ridge that could promote a large flux of dFe toward upper waters. This study confirms that short-lived radium isotopes are powerful tracers of hydrothermal plumes associated with slow-rate spreading ridges and supports the importance of low-expansion-rate ridges as significant sources of dFe to the deep ocean. However, a more detailed study should be organized in order to better constrain the exact location of the hydrothermal activity and the fate of the associate plume, to confirm the first results obtained here.

Acknowledgments

The authors thank the captain and the crew of the R/V Marion Dufresne for their assistance during the SWINGS cruise. The authors also thank Emmanuel de Saint-Léger and Fabien Pérault, Marion Lagarde, Nolwenn Lemaitre, Edwin Cotard, Frederic Planchon for their help during the deployment of the *in-situ* pumps. We are grateful to Gérard Eldin, Sara Sergi, Corentin Clerc and Loyd Izard for CTD data acquisition and preparation of Niskin bottles. We thank Anne Briais, Cédric Boulart, Cyrille Poncelet, Carla Scalabrin, Hervé Bisquay, Cedric Cotté and Lloyd Izard for the hydrothermal survey and to Thomas Zambardi for his help at the LAFARA underground laboratory. The help of Eric Greiner (Mercator Ocean International) who provided state of the art GLORYS12 simulations is gratefully acknowledged. The authors also thank Sebastien Hervé for his talent as a graphic facilitator and Antonin Soulié for his Python skills. The SWINGS project was supported by the French Oceanographic Fleet, ANR (Agence Nationale de la Recherche ; ANR) CNRS/ INSU (Centre Nationale de la Recherche Scientifique/Institut National des Sciences de l'Univers) and ISblue (ANR-17-EURE-0015*).* This study has been partially supported through the grant EUR TESS N°ANR-18-EURE-0018 in the framework of the Programme des Investissements d'Avenir. The authors thank Reiner Schlitzer for the Ocean Data View software (https://odv.awi.de, 2020) and R Pawlowicz for the M_Map Matlab toolbox. The GEOTRACES 2021 Intermediate Data Product (IDP 2021) represents an international collaboration and is endorsed by the Scientific Committee on Oceanic Research (SCOR). M.A.C. was funded by the National Science Foundation Chemical Oceanography program (OCE-1829431). The many researchers and funding agencies responsible for the collection of data and quality control are thanked for their contribution to the IDP2021.

Author contributions

CJ and HP wrote the proposal to secure fundings for the project and were co-PIs of the SWINGS cruise. The sampling design for fieldwork was conducted by HP, CJ, PvB, VS and FV. PvB, MS, ML, HP and CC mobilized equipment and consumables for fieldwork. Samples were collected in the field by PvB, VS, ML, HP and CB. Sample analysis was conducted by PvB, VS, ML, MS, MAC, HP and CC. FV and EK worked on the physical modeling and observation part. ML, PvB and VS analyzed and interpreted the data, ML produced the figures and wrote the paper. All authors provided comments on subsequent drafts of the paper.

References

Anderson, R.F., Bacon, M.P., Brewer, P.G., 1983. Removal of230Th and231Pa from the open ocean. Earth Planet. Sci. Lett. 62, 7–23. https://doi.org/10.1016/0012-821X(83)90067-5

Ardyna, M., Lacour, L., Sergi, S., d'Ovidio, F., Sallée, J.-B., Rembauville, M., Blain, S., Tagliabue, A., Schlitzer, R., Jeandel, C., Arrigo, K.R., Claustre, H., 2019. Hydrothermal vents trigger massive phytoplankton blooms in the Southern Ocean. Nat. Commun. 10, 2451.

Baker et al., 2004, Geochem. Geophys. Geosyst, 5, Q08002, Hydrothermal venting in magma deserts: The ultraslow-spreading Gakkel and Southwest Indian Ridges, doi:10.1029/2004GC000712.

Baker, E.T., German, C.R., Elderfield, H., 2013. Hydrothermal Plumes Over Spreading-Center Axes: Global Distributions and Geological Inferences, in: Humphris, S.E., Zierenberg, R.A., Mullineaux, L.S., Thomson, R.E. (Eds.), Geophysical Monograph Series. American Geophysical Union, Washington, D. C., pp. 47–71. https://doi.org/10.1029/GM091p0047

Baskaran, M., Murphy, D.J., Santschi, P.H., Orr, J.C., Schink, D.R., 1993. A method for rapid in situ extraction and laboratory determination of Th, Pb, and Ra isotopes from large volumes of seawater. Deep Sea Res. Part Oceanogr. Res. Pap. 40, 849–865. https://doi.org/10.1016/0967-0637(93)90075-E

Blain, S., Quéguiner, B., Armand, L., Belviso, S., Bombled, B., Bopp, L., Bowie, A., Brunet, C., Brussaard, C., Carlotti, F., Christaki, U., Corbière, A., Durand, I., Ebersbach, F., Fuda, J.-L., Garcia, N., Gerringa, L., Griffiths, B., Guigue, C., Guillerm, C., Jacquet, S., Jeandel, C., Laan, P., Lefèvre, D., Lo Monaco, C., Malits, A., Mosseri, J., Obernosterer, I., Park, Y.-H., Picheral, M., Pondaven, P., Remenyi, T., Sandroni, V., Sarthou, G., Savoye, N., Scouarnec, L., Souhaut, M., Thuiller, D., Timmermans, K., Trull, T., Uitz, J., van Beek, P., Veldhuis, M., Vincent, D., Viollier, E., Vong, L., Wagener, T., 2007. Effect of natural iron fertilization on carbon sequestration in the Southern Ocean. Nature 446, 1070–1074. https://doi.org/10.1038/nature05700

Boyd, P.W., Ellwood, M.J., 2010. The biogeochemical cycle of iron in the ocean. Nat. Geosci. 3, 675–682. https://doi.org/10.1038/ngeo964

Buck, N.J., Resing, J.A., Baker, E.T., Lupton, J.E., 2018. Chemical Fluxes From a Recently Erupted Shallow Submarine Volcano on the Mariana Arc. Geochem. Geophys. Geosystems 19, 1660–1673. https://doi.org/10.1029/2018GC007470

Campbell, A.C., Palmer, M.R., Klinkhammer, G.P., Bowers, T.S., Edmond, J.M., Lawrence, J.R., Casey, J.F., Thompson, G., Humphris, S., Rona, P., Karson, J.A., 1988. Chemistry of hot springs on the Mid-Atlantic Ridge. Nature 335, 514–519. https://doi.org/10.1038/335514a0

Charette, M.A., Gonneea, M.E., Morris, P.J., Statham, P., Fones, G., Planquette, H., Salter, I., Garabato, A.N., 2007. Radium isotopes as tracers of iron sources fueling a Southern Ocean phytoplankton bloom. Deep Sea Res. Part II Top. Stud. Oceanogr. 54, 1989–1998. https://doi.org/10.1016/j.dsr2.2007.06.003

Chase, Z., Anderson, R.F., Fleisher, M.Q., Kubik, P.W., 2003. Scavenging of 230Th, 231Pa and 10Be in the Southern Ocean (SW Pacific sector): the importance of particle flux, particle composition and advection. Deep Sea Res. Part II Top. Stud. Oceanogr. 50, 739–768. https://doi.org/10.1016/S0967-0645(02)00593-3

Chen, J., Tao, C., Liang, J., Liao, S., Dong, C., Li, H., Li, W., Wang, Y., Yue, X., He, Y., 2018. Newly discovered hydrothermal fields along the ultraslow-spreading Southwest Indian Ridge around 63°E. Acta Oceanol. Sin. 37, 61–67. https://doi.org/10.1007/s13131-018-1333-y

Chung, Y., 1987. 226Ra in the western Indian Ocean. Earth Planet. Sci. Lett. 85, 11–27. https://doi.org/10.1016/0012-821X(87)90017-3

Cochran, J.K., 1982. The oceanic chemistry of the U- and Th-series nuclides.

Colbert, S.L., Hammond, D.E., 2007. Temporal and spatial variability of radium in the coastal ocean and its impact on computation of nearshore cross-shelf mixing rates. Cont. Shelf Res. 27, 1477–1500. https://doi.org/10.1016/j.csr.2007.01.003

Corliss, J.B., Dymond, J., Gordon, L.I., Edmond, J.M., Von Herzen, R.P., Ballard, R.D., Green, K., Williams, D., Bainbridge, A., Crane, K., Van Andel, T.H., 1979. Submarine Thermal Springs on the Galápagos Rift. Science 203, 1073–1083. https://doi.org/10.1126/science.203.4385.1073

Edmond, J.M., Measures, C., McDuff, R.E., Chan, L.H., Collier, R., Grant, B., Gordon, L.I., Corliss, J.B., 1979. Ridge crest hydrothermal activity and the balances of the major and minor elements in the ocean: The Galapagos data. Earth Planet. Sci. Lett. 46, 1–18. https://doi.org/10.1016/0012-821X(79)90061-X

Edmond, J.M., Von Damm, K.L., McDuff, R.E., Measures, C.I., 1982. Chemistry of hot springs on the East Pacific Rise and their effluent dispersal. Nature 297, 187–191. https://doi.org/10.1038/297187a0

Egbert, G. D., Erofeeva, S. Y., 2002. Efficient inverse modeling of barotropic ocean tides. Journal of Atmospheric and Oceanic Technology, 19 (2), 183 – 204. doi: 10.1175/1520-0426(2002)019h0183:EIMOBOi2.0.CO;2

Elderfield, H., Schultz, A., 1996. Mid-Ocean Ridge Hydrothermal Fluxes and the Chemical Composition of the Ocean. Annu. Rev. Earth Planet. Sci. 24, 191–224. https://doi.org/10.1146/annurev.earth.24.1.191

Garcia-Orellana, J., Rodellas, V., Tamborski, J., Diego-Feliu, M., van Beek, P., Weinstein, Y., Charette, M., Alorda-Kleinglass, A., Michael, H.A., Stieglitz, T., Scholten, J., 2021. Radium isotopes as submarine groundwater discharge (SGD) tracers: Review and recommendations. Earth-Sci. Rev. 220, 103681. https://doi.org/10.1016/j.earscirev.2021.103681

Garcia-Solsona, E., Garcia-Orellana, J., Masqué, P., Dulaiova, H., 2008. Uncertainties associated with 223Ra and 224Ra measurements in water via a Delayed Coincidence Counter (RaDeCC). Mar. Chem. 22.

Geibert, W., Charette, M., Kim, G., Moore, W.S., Street, J., Young, M., Paytan, A., 2008. The release of dissolved actinium to the ocean: A global comparison of different end-members. Mar. Chem. 109, 409–420. https://doi.org/10.1016/j.marchem.2007.07.005

German, C.R., Baker, E.T., Mevel, C., Tamaki, K., The Fuji Science Team, 1998. Hydrothermal activity along the southwest Indian ridge. Nature 395, 490–493. https://doi.org/10.1038/26730

German, C.R., Seyfried, W.E., 2014. Hydrothermal Processes, in: Treatise on Geochemistry. Elsevier, pp. 191–233. https://doi.org/10.1016/B978-0-08-095975-7.00607-0

German, C.R., Von Damm, K.L., 2003. Hydrothermal Processes, in: Treatise on Geochemistry. Elsevier, pp. 181–222. https://doi.org/10.1016/B0-08-043751-6/06109-0

German, C.R., Thurnherr, A.M., Knoery, J., Charlou, J.-L., Jean-Baptiste, P., Edmonds, H.N., 2010. Heat, volume and chemical fluxes from submarine venting: A synthesis of results from the Rainbow hydrothermal field, 36°N MAR. Deep Sea Res. Part Oceanogr. Res. Pap. 57, 518–527. https://doi.org/10.1016/j.dsr.2009.12.011

Hammond, D.E., Zukin, J.G., Ku, T.-L., 1988. The kinetics of radioisotope exchange between brine and rock in a geothermal system. J. Geophys. Res. Solid Earth 93, 13175–13186. https://doi.org/10.1029/JB093iB11p13175

Han, X., Wu, G., Cui, R., Qiu, Z., Deng, X., Wang, Y., Scientific Party Of Dy115-21 Cruise Leg 7, 2010. Discovery of a Hydrothermal Sulfide Deposit on the Southwest Indian Ridge at 49.2°E 2010, OS21C-1531.

Hancock, G.J., Webster, Ian.T., Stieglitz, T.C., 2006. Horizontal mixing of Great Barrier Reef waters: Offshore diffusivity determined from radium isotope distribution. J. Geophys. Res. 111, C12019. https://doi.org/10.1029/2006JC003608Henderson, P.B., Morris, P.J., Moore, W.S., Charette, M.A., 2013. Methodological advances for measuring low-level radium isotopes in seawater. J. Radioanal. Nucl. Chem. 296, 357–362. https://doi.org/10.1007/s10967-012-2047-9

HUMLER Eric, 2001. MD 121 / SWIFT cruise,Marion Dufresne R/V. https://doi.org/10.17600/1200030

Humphris, S.E., Zierenberg, R.A., Mullineaux, L.S., Thomson, R.E. (Eds.), 1995. Seafloor Hydrothermal Systems: Physical, Chemical, Biological, and Geological Interactions: Humphris/Seafloor Hydrothermal Systems: Physical, Chemical, Biological, and Geological Interactions, Geophysical Monograph Series. American Geophysical Union, Washington, D. C. https://doi.org/10.1029/GM091

Inoue, M., Hanaki, S., Kameyama, H., Kumamoto, Y., Nagao, S., 2022. Unique current connecting Southern and Indian Oceans identified from radium distributions. Sci. Rep. 12, 1781. https://doi.org/10.1038/s41598-022-05928-y

Intermediate Data Product Group, 2021. The GEOTRACES Intermediate Data Product 2021 (IDP2021). https://doi.org/10.5285/CF2D9BA9-D51D-3B7C-E053-8486ABC0F5FD

Kadko, D., 1996. Radioisotopic studies of submarine hydrothermal vents. Rev. Geophys. 34, 349–366. https://doi.org/10.1029/96RG01762

Kadko, D., Butterfield, D.A., 1998. The relationship of hydrothermal fluid composition and crustal residence time to maturity of vent fields on the Juan de Fuca Ridge. Geochim. Cosmochim. Acta 62, 1521–1533. https://doi.org/10.1016/S0016-7037(98)00088-X

Kadko, D., Gronvold, K., Butterfield, D., 2007. Application of radium isotopes to determine crustal residence times of hydrothermal fluids from two sites on the Reykjanes Peninsula, Iceland. Geochim. Cosmochim. Acta 71, 6019–6029. https://doi.org/10.1016/j.gca.2007.09.018

Kadko, D., Moore, W., 1988. Radiochemical constraints on the crustal residence time of submarine hydrothermal fluids: Endeavour Ridge. Geochim. Cosmochim. Acta 52, 659–668. https://doi.org/10.1016/0016-7037(88)90328-6

Keir, R.S., Schmale, O. , Walter, M. , Sülltenfuß, J. , Seifert, R., Rhein, M., 2008. Flux and dispersion of gases from the "Drachenschlund" hydrothermal vent at 8° 18′ S, 13° 30′ W on the Mid-Atlantic Ridge. Earth and Planetary Science Letters, 270 (2008), pp. 338-348. https://doi.org/10.1016/j.epsl.2008.03.054
Kipp, L.E., Charette, M.A., Hammond, D.E., Moore, W.S., 2015. Hydrothermal vents: A previously unrecognized source of actinium-227 to the deep ocean. Mar. Chem. 177, 583–590. https://doi.org/10.1016/j.marchem.2015.09.002

Kipp, L.E., Sanial, V., Henderson, P.B., van Beek, P., Reyss, J.-L., Hammond, D.E., Moore, W.S., Charette, M.A., 2018. Radium isotopes as tracers of hydrothermal inputs and neutrally buoyant plume dynamics in the deep ocean. Mar. Chem. 201, 51–65. https://doi.org/10.1016/j.marchem.2017.06.011

Koch-Larrouy, A., Atmadipoera, A., van Beek, P., Madec, G., Aucan, J., Lyard, F., Grelet, J., Souhaut, M., 2015. Estimates of tidal mixing in the Indonesian archipelago from multidisciplinary INDOMIX in-situ data. Deep Sea Res. Part Oceanogr. Res. Pap. 106, 136–153. https://doi.org/10.1016/j.dsr.2015.09.007

Krishnaswami, S., Graustein, W.C., Turekian, K.K., Dowd, J.F., 1982. Radium, thorium, and radioactive lead isotopes in ground waters: application to the in-situ determination of adsorption rate constants and retardation factors. Water Resour. Res. 18, 1663–1675.

Ku, T.L., Li, Y.H., Mathieu, G.G., Wong, H.K., 1970. Radium in the Indian-Antarctic Ocean south of Australia. J. Geophys. Res. 75, 5286–5292. https://doi.org/10.1029/JC075i027p05286

Ku, T.-L., Lin, M.-C., 1976. 226Ra distribution in the Antarctic Ocean. Earth Planet. Sci. Lett. 32, 236–248. https://doi.org/10.1016/0012-821X(76)90064-9

Ku, T.-L., Luo, S., 1994. New appraisal of radium 226 as a large-scale oceanic mixing tracer. J. Geophys. Res. 99, 10255. https://doi.org/10.1029/94JC00089

Lamontagne, S., Le Gal La Salle, C., Hancock, G.J., Webster, I.T., Simmons, C.T., Love, A.J., James-Smith, J., Smith, A.J., Kämpf, J., Fallowfield, H.J., 2008. Radium and radon radioisotopes in regional groundwater, intertidal groundwater, and seawater in the Adelaide Coastal Waters Study area: Implications for the evaluation of submarine groundwater discharge. Mar. Chem. 109, 318–336. https://doi.org/10.1016/j.marchem.2007.08.010

Law, C.S., Abraham, E.R., Watson, A., Liddicoat, M., 2003. Vertical eddy diffusion and nutrient supply to the surface mixed layer of the Antarctic Circumpolar Current. J. Geophys. Res. 108, 3272. https://doi.org/10.1029/2002JC001604

Lellouche, J.-M., Greiner, E., Bourdallé-Badie, R., Garric, G., Melet, A., Drévillon, M., Bricaud C., Hamon, M., Le Galloudec, O., Regnier, C., Candela, T., Testut, C.-E., Gasparin, F., Ruggiero, G., Benkiran, M., Drillet, Y., Le Traon, P.-Y. (2021). The Copernicus Global 1/12°

Oceanic and Sea Ice GLORYS12 Reanalysis. *Front. Earth Sci.* 9:698876. doi: 10.3389/feart.2021.698876

Le Roy, E., Sanial, V., Lacan, F., van Beek, P., Souhaut, M., Charette, M.A., Henderson, P.B., 2019. Insight into the measurement of dissolved 227Ac in seawater using radium delayed coincidence counter. Mar. Chem. 212, 64–73. https://doi.org/10.1016/j.marchem.2019.04.002

Lemaitre, N., de Souza, G.F., Archer, C., Wang, R.-M., Planquette, H., Sarthou, G., Vance, D., 2020. Pervasive sources of isotopically light zinc in the North Atlantic Ocean. Earth Planet. Sci. Lett. 539, 116216. https://doi.org/10.1016/j.epsl.2020.116216

Léon, M., Van Beek, P., Sanial, V., Souhaut, M., Henderson, P., Charette, M.A., 2024. Comparison of methods to determine extraction efficiencies of Ra isotopes and 227Ac from large volume seawater samples. Marine Chemistry 258, 104328. https://doi.org/10.1016/j.marchem.2023.104328

Li, Y.-H., Feely, H.W., Toggweiler, J.R., 1980. 228Ra and 228Th concentrations in GEOSECS Atlantic surface waters. Deep Sea Res. Part Oceanogr. Res. Pap. 27, 545–555. https://doi.org/10.1016/0198-0149(80)90039-4

Liao, S., Tao, C., Li, H., Zhang, G., Liang, J., Yang, W., Wang, Y., 2018. Surface sediment geochemistry and hydrothermal activity indicators in the Dragon Horn area on the Southwest Indian Ridge. Marine Geology 398, 22–34. https://doi.org/10.1016/j.margeo.2017.12.005

Livingston, H.D., Cochran, J.K., 1987. Determination of transuranic and thorium isotopes in ocean water: In solution and in filterable particles. J. Radioanal. Nucl. Chem. Artic. 115, 299–308. https://doi.org/10.1007/BF02037445

Lough, A.J.M., Tagliabue, A., Demasy, C., Resing, J.A., Mellett, T., Wyatt, N.J., Lohan, M.C., 2023. Tracing differences in iron supply to the Mid-Atlantic Ridge valley between hydrothermal vent sites: implications for the addition of iron to the deep ocean. Biogeosciences 20, 405–420. https://doi.org/10.5194/bg-20-405-2023

Mann, D.R., Casso, S.A., 1984. In situ chemisorption of radiocesium from seawater. Mar. Chem. 14, 307–318. https://doi.org/10.1016/0304-4203(84)90027-6

Massoth, G.J., Baker, E.T., Lupton, J.E., Feely, R.A., Butterfield, D.A., Von Damm, K.L., Roe, K.K., Lebon, G.T., 1994. Temporal and spatial variability of hydrothermal manganese and iron at Cleft segment, Juan de Fuca Ridge. J. Geophys. Res. Solid Earth 99, 4905–4923. https://doi.org/10.1029/93JB02799

Moore, W., 1972. Radium-228: Application to thermocline mixing studies. Earth Planet. Sci. Lett. 16, 421–422. https://doi.org/10.1016/0012-821X(72)90161-6

Moore, W.S., 2008. Fifteen years experience in measuring 224Ra and 223Ra by delayed-coincidence counting. Mar. Chem. 109, 188–197. https://doi.org/10.1016/j.marchem.2007.06.015

Moore, W.S., 2000a. Determining coastal mixing rates using radium isotopes. Cont. Shelf Res. 20, 1993–2007. https://doi.org/10.1016/S0278-4343(00)00054-6

Moore, W.S., 2000b. Ages of continental shelf waters determined from ^{223}Ra and ^{224}Ra. J. Geophys. Res. 105, 22117–22122. https://doi.org/10.1029/1999JC000289

Moore, W.S., Cai, P., 2013. Calibration of RaDeCC systems for 223Ra measurements. Mar. Chem. 156, 130–137. https://doi.org/10.1016/j.marchem.2013.03.002

Moore, W.S., de Oliveira, J., 2008. Determination of residence time and mixing processes of the Ubatuba, Brazil, inner shelf waters using natural Ra isotopes. Estuar. Coast. Shelf Sci. 76, 512–521. https://doi.org/10.1016/j.ecss.2007.07.042

Moore, W.S., Frankle, J.D., Benitez-Nelson, C.R., Früh-Green, G.L., Lang, S.Q., 2021. Activities of ^{223}Ra and ^{226}Ra in Fluids From the Lost City Hydrothermal Field Require Short Fluid Residence Times. J. Geophys. Res. Oceans 126. https://doi.org/10.1029/2021JC017886

Moore, W.S., Reid, D.F., 1973. Extraction of radium from natural waters using manganese-impregnated acrylic fibers. J. Geophys. Res. 78, 8880–8886. https://doi.org/10.1029/JC078i036p08880

Moore, W.S., Ussler, W., Paull, C.K., 2008. Short-lived radium isotopes in the Hawaiian margin: Evidence for large fluid fluxes through the Puna Ridge. Mar. Chem. 109, 421–430. https://doi.org/10.1016/j.marchem.2007.09.010

Neuholz, R., Schnetger, B., Kleint, C., Koschinsky, A., Lettmann, K., Sander, S., Türke, A., Walter, M., Zitoun, R., Brumsack, H.-J., 2020a. Near-field hydrothermal plume dynamics at Brothers Volcano (Kermadec Arc): A short-lived radium isotope study. Chem. Geol. 533, 119379. https://doi.org/10.1016/j.chemgeo.2019.119379

Neuholz R, Kleint C, Schnetger B, Koschinsky A, Laan P, Middag R, Sander S, Thal J, Türke A, Walter M, Zitoun R, Brumsack H-J; 2020b Submarine Hydrothermal Discharge and Fluxes of Dissolved Fe and Mn, and He Isotopes at Brothers Volcano Based on Radium Isotopes. Minerals 10, 969.

Nozaki, Y., 1993. Actinium-227: A Steady State Tracer for the Deep-sea Basin-wide Circulation and Mixing Studies, in: Elsevier Oceanography Series. Elsevier, pp. 139–156. https://doi.org/10.1016/S0422-9894(08)71323-0

Nozaki, Y., 1984. Excess 227Ac in deep ocean water. Nature 310, 486–488. https://doi.org/10.1038/310486a0

Park, Y.-H., Gamberoni, L., 1997. Cross-frontal exchange of Antarctic Intermediate Water and Antarctic Bottom Water in the Crozet Basin. Deep Sea Res. Part II Top. Stud. Oceanogr. 44, 963–986. https://doi.org/10.1016/S0967-0645(97)00004-0

Patriat, P., Sauter, D., Munschy, M., Parson, L., 1997. A Survey of the Southwest Indian Ridge Axis Between Atlantis II Fracture Zone and the Indian Ocean Triple Junction: Regional Setting

and Large Scale Segmentation. Mar. Geophys. Res. 19, 457–480. https://doi.org/10.1023/A:1004312623534

Ramirez-Llodra, E., Brandt, A., Danovaro, R., De Mol, B., Escobar, E., German, C.R., Levin, L.A., Martinez Arbizu, P., Menot, L., Buhl-Mortensen, P., Narayanaswamy, B.E., Smith, C.R., Tittensor, D.P., Tyler, P.A., Vanreusel, A., Vecchione, M., 2010. Deep, diverse and definitely different: unique attributes of the world's largest ecosystem. Biogeosciences 7, 2851–2899. https://doi.org/10.5194/bg-7-2851-2010

Resing, J.A., Sedwick, P.N., German, C.R., Jenkins, W.J., Moffett, J.W., Sohst, B.M., Tagliabue, A., 2015. Basin-scale transport of hydrothermal dissolved metals across the South Pacific Ocean. Nature 523, 200–203. https://doi.org/10.1038/nature14577

Rudnicki, M.D., James, R.H., Elderfield, H., 1994. Near-field variability of the TAG non-buoyant plume, 26°N, Mid-Atlantic Ridge. Earth Planet. Sci. Lett. 127, 1–10. https://doi.org/10.1016/0012-821X(94)90193-7

Saito, M.A., Noble, A.E., Tagliabue, A., Goepfert, T.J., Lamborg, C.H., Jenkins, W.J., 2013. Slow-spreading submarine ridges in the South Atlantic as a significant oceanic iron source. Nat. Geosci. 6, 775–779. https://doi.org/10.1038/ngeo1893

Sanial, V., van Beek, P., Lansard, B., d'Ovidio, F., Kestenare, E., Souhaut, M., Zhou, M., Blain, S., 2014. Study of the phytoplankton plume dynamics off the Crozet Islands (Southern Ocean): A geochemical-physical coupled approach. J. Geophys. Res. Oceans 119, 2227–2237. https://doi.org/10.1002/2013JC009305

Sanial, V., van Beek, P., Lansard, B., Souhaut, M., Kestenare, E., d'Ovidio, F., Zhou, M., Blain, S., 2015. Use of Ra isotopes to deduce rapid transfer of sediment-derived inputs off Kerguelen. Biogeosciences 12, 1415–1430. https://doi.org/10.5194/bg-12-1415-2015

Sarmiento, J.L., Rooth, C.G.H., Broecker, W.S., 1982. Radium 228 as a tracer of basin wide processes in the abyssal ocean. J. Geophys. Res. 87, 9694. https://doi.org/10.1029/JC087iC12p09694

Sarthou, G., Vincent, D., Christaki, U., Obernosterer, I., Timmermans, K.R., Brussaard, C.P.D., 2008. The fate of biogenic iron during a phytoplankton bloom induced by natural fertilisation: Impact of copepod grazing. Deep Sea Res. Part II Top. Stud. Oceanogr. 55, 734–751. https://doi.org/10.1016/j.dsr2.2007.12.033

Sato, T., Okino, K., Sato, H., Mizuno, M., Hanyu, T., Seama, N., 2013. Magmatic activities on the Southwest Indian Ridge between 35°E and 40°E, the closest segment to the Marion hotspot. Geochemistry, Geophysics, Geosystems 14, 5286–5307. https://doi.org/10.1002/2013GC004814

Sauter, D. and Cannat, M., 2010. The ultraslow spreading Southwest Indian ridge. *Diversity of hydrothermal systems on slow spreading ocean ridges*, *88*, pp.153-173.

Schine, C.M.S., Alderkamp, A.-C., van Dijken, G., Gerringa, L.J.A., Sergi, S., Laan, P., van Haren, H., van de Poll, W.H., Arrigo, K.R., 2021. Massive Southern Ocean phytoplankton bloom

fed by iron of possible hydrothermal origin. Nat. Commun. 12, 1211. https://doi.org/10.1038/s41467-021-21339-5

St Laurent, L.C., Thurnherr, A.M., 2007. Intense mixing of lower thermocline water on the crest of the Mid-Atlantic Ridge. Nature 448, 680–683. https://doi.org/10.1038/nature06043

Stachelhaus, S.L., Moran, S.B., 2012. A simple differential diffusion model to account for the discrepancy between ^{223}Ra- and ^{224}Ra-based eddy diffusivities: DIFFERENTIAL DIFFUSION AND Ra-BASED *K*. J. Geophys. Res. Oceans 117, n/a-n/a. https://doi.org/10.1029/2011JC007500

Tagliabue, A., Bopp, L., Dutay, J.-C., Bowie, A.R., Chever, F., Jean-Baptiste, P., Bucciarelli, E., Lannuzel, D., Remenyi, T., Sarthou, G., Aumont, O., Gehlen, M., Jeandel, C., 2010. Hydrothermal contribution to the oceanic dissolved iron inventory. Nat. Geosci. 3, 252–256. https://doi.org/10.1038/ngeo818

Tagliabue, A., Sallée, J.-B., Bowie, A.R., Lévy, M., Swart, S., Boyd, P.W., 2014. Surface-water iron supplies in the Southern Ocean sustained by deep winter mixing. Nat. Geosci. 7, 314–320. https://doi.org/10.1038/ngeo2101

Tagliabue, A., Lough, A.J.M., Vic, C., Roussenov, V., Gula, J., Lohan, M.C., Resing, J.A., Williams, R.G., 2022. Mechanisms Driving the Dispersal of Hydrothermal Iron From the Northern Mid Atlantic Ridge. Geophys. Res. Lett. 49. https://doi.org/10.1029/2022GL100615

Tao, C., Guo, Z., Liang, J., Ding, T., Yang, W., Liao, S., Chen, M., Zhou, F., Chen, J., Wang, N., Liu, X., Zhou, J., 2023. Sulfide metallogenic model for the ultraslow-spreading Southwest Indian Ridge. Sci. China Earth Sci. 66, 1212–1230. https://doi.org/10.1007/s11430-023-1108-7

Tao, C., Li, H., Zhou, J., Wu, T., He, Y., Deng, X., Zhang, G., Liu, W., 2014. Seafloor hydrothermal activity and polymetallic sulfide exploration on the southwest Indian ridge. Chinese Science Bulletin 59, 2266–2276. https://doi.org/10.1007/s11434-014-0182-0

Tao, C., Lin, J., Guo, S., Chen, Y.J., Wu, G., Han, X., German, C.R., Yoerger, D.R., Zhou, N., Li, H., Su, X., Zhu, J., and the DY115-19 (Legs 1–2) and DY115-20 (Legs 4–7) Science Parties, 2012. First active hydrothermal vents on an ultraslow-spreading center: Southwest Indian Ridge. Geology 40, 47–50. https://doi.org/10.1130/G32389.1

Tao, C., Wu, G., Ni, J., Zhao, H., Su, X., Zhou, N., Li, J., Chen, Y., Cui, R., Deng, X., Egorov, I., Dobretsova, I., Sun, G., Qiu, Z., Zhou, J., Gu, C., Yang, J., Zhang, K., Wu, X., Lin, J., 2009. New hydrothermal fields found along the SWIR during the Legs 5-7 of the Chinese DY115-20 Expedition. AGU Fall Meeting Abstracts 1150.

Thomas, A.L., Henderson, G.M., Robinson, L.F., 2006. Interpretation of the 231Pa/230Th paleocirculation proxy: New water-column measurements from the southwest Indian Ocean. Earth Planet. Sci. Lett. 241, 493–504. https://doi.org/10.1016/j.epsl.2005.11.031

Thurnherr, A.M., Richards, K.J., German, C.R., Lane-Serff, G.F., Speer, K.G., 2002. Flow and Mixing in the Rift Valley of the Mid-Atlantic Ridge. J. Phys. Oceanogr. 32, 1763–1778. https://doi.org/10.1175/1520-0485(2002)032<1763:FAMITR>2.0.CO;2

Tonnard, M., Planquette, H., Bowie, A.R., van der Merwe, P., Gallinari, M., Desprez de Gésincourt, F., Germain, Y., Gourain, A., Benetti, M., Reverdin, G., Tréguer, P., Boutorh, J., Cheize, M., Lacan, F., Menzel Barraqueta, J.-L., Pereira-Contreira, L., Shelley, R., Lherminier, P., Sarthou, G., 2020. Dissolved iron in the North Atlantic Ocean and Labrador Sea along the GEOVIDE section (GEOTRACES section GA01). Biogeosciences 17, 917–943. https://doi.org/10.5194/bg-17-917-2020

van Beek, P., Bourquin, M., Reyss, J.-L., Souhaut, M., Charette, M.A., Jeandel, C., 2008. Radium isotopes to investigate the water mass pathways on the Kerguelen Plateau (Southern Ocean). Deep Sea Res. Part II Top. Stud. Oceanogr. 55, 622–637. https://doi.org/10.1016/j.dsr2.2007.12.025

van Beek, P., Souhaut, M., Lansard, B., Bourquin, M., Reyss, J.-L., von Ballmoos, P., Jean, P., 2013. LAFARA: a new underground laboratory in the French Pyrénées for ultra low-level gamma-ray spectrometry. J. Environ. Radioact. 116, 152–158. https://doi.org/10.1016/j.jenvrad.2012.10.002

van der Loeff, M.M.R., Moore, W.S., 1999. Determination of natural radioactive tracers, in: Grasshoff, K., Kremling, K., Ehrhardt, M. (Eds.), Methods of Seawater Analysis. Wiley-VCH Verlag GmbH, Weinheim, Germany, pp. 365–397. https://doi.org/10.1002/9783527613984.ch13

Visbeck, M. (2002), Deep velocity profiling using Lowered Acoustic Doppler Current Profilers: bottom track and inverse solutions, J. Atm. Ocean. Tech., *19*, 794-807.

Von Damm, K.L., 1990. SEAFLOOR HYDROTHERMAL ACTIVITY: BLACK SMOKER CHEMISTRY AND CHIMNEYS. Annu. Rev. Earth Planet. Sci. 18, 173–204. https://doi.org/10.1146/annurev.ea.18.050190.001133

Walter, M., Mertens, C., Stöber, U., German, C.R., Yoerger, D.R., Sültenfuß, J., Rhein, M., Melchert, B., Baker, E.T., 2010. Rapid dispersal of a hydrothermal plume by turbulent mixing. Deep Sea Research Part I: Oceanographic Research Papers 57, 931–945. https://doi.org/10.1016/j.dsr.2010.04.010

Wolery, T.J., Sleep, N.H., 1976. Hydrothermal Circulation and Geochemical Flux at Mid-Ocean Ridges. J. Geol. 84, 249–275. https://doi.org/10.1086/628195

Figure Caption:

Table 1: Radium activities at stations 14 and 15, "<DL" indicates activities below detection limit. Here we report i) the Ra activity ratios determined in Mn-cartridges, ii) Ra activities determined using Mn-fibers and iii) Ra activities in seawater determined by combining the ^{226}Ra activities determined using Mn-fibers and the activity ratios determined using Mn-cartridges.

Table 2: ^{227}Ac activities, in dpm 100L^{-1}, at stations 14 and 15.

Figure 1. High resolution (15 m) bathymetry map of the SWIR segment investigated during SWINGS cruise. The locations of stations 14 and 15 are shown as black triangles on the map. The location of the segment is shown on the bottom left panel (black square). The color bar shows the bathymetry that ranges from 862.8 to 2835.7 m.

Figure 2: Temperature (grey full line), salinity (black full line), beam transmission (black dotted line) and oxygen (grey dashed line) profiles at stations 14 (left panel) and 15 (right panel). The horizontal black lines represent the bottom depth for each Station.

Figure 3. Map of horizontal currents averaged between January 25 and January 29, 2021, from satellite altimetry (a.) and from the GLORYS12 reanalysis at 190 m (b), 1250 m (c) and 1450 m (d). The black line denotes the 2000 m isobath. The location of Stations 14 and 15 is indicated by magenta triangles. Units in m s^{-1}.

Figure 4. Horizontal currents at depths below 1000 m measured by the LADCP at station 14 on 28 January 2021 and at station 15 on 29 January. A second LADCP cast was performed at Station 14 on 28 January, denoted by thin arrows. Green arrows denote the barotropic tidal current at the time of the cast according to the TPXO9v5 model. Corresponding variance ellipses for the dominant M2 constituent computed between 27 January and 2 February are also shown. Current velocity on 28 January from the GLORYS12 reanalysis are shown at a depth of 1250 m and 1450 m (where applicable): red dots denote model grid points. Bathymetry is from the multibeam echo sounder (contour interval 50 m), with the 1250 m isobath highlighted. Unit for the velocity is cm s^{-1} (velocity scale in the top right corner).

Figure 5. $^{223}Ra_{ex}$ and $^{224}Ra_{ex}$ activities are shown as black circles and black triangles, respectively. Filled symbols represent activities determined by combining the activities determined using Mn-fibers and Mn-cartridges, while open symbols represent activities determined in the Mn-fibers. The graph in the right panel in grey shows, as a comparison, the vertical profiles observed off Kerguelen islands with grey triangle as $^{224}Ra_{ex}$ and grey dots as $^{223}Ra_{ex}$ (Sanial et al., 2015). Errors bars are reported but are often within the symbol. The horizontal lines represent the depth of the seafloor.

Figure 6. ^{227}Ac activities are shown as black circles. The horizontal lines represent the depth of the seafloor.

Figure 7. ^{226}Ra and ^{228}Ra activities are shown as white diamonds and black triangles, respectively. The horizontal lines represent the depth of the seafloor. Errors bars for ^{226}Ra are reported but are often within the symbol.

Figure 8. Conceptual figure illustrating the circulation of the fluid within a hydrothermal system and the associated partitioning of radionuclides from the U-Th decay chain.

Figure 9. Vertical eddy diffusivity coefficient (K_Z) estimation at station 14 using a simple one-dimensional diffusion model applied to the vertical profiles of $^{223}Ra_{ex}$ (left panel) and $^{224}Ra_{ex}$ (right panel). The best exponential fits considering Ra data in the 1000–1250 m depth interval together with the R value are reported. The horizontal lines represent the depth of the seafloor. The uncertainties on the K_Z are derived from the uncertainty on the best exponential fit coefficient of Ra activities as function of distance from bottom (Equation 2).

All authors declare that they have no conflicts of interest.

- Short-lived Ra isotopes highlight the presence of a hydrothermal activity on the SWIR
- The hydrothermal system is located at a distance < 30km of the investigated stations
- A strong vertical mixing is observed (Kz from 38 up to 149 $cm^2\ s^{-1}$)
- A large dFe vertical flux from 552 up to1173 nmol $m^{-2}\ d^{-1}$ are estimated